

Spatio-temporal analysis of extreme winter temperatures in Ireland

Dáire Healy¹, Jonathan A. Tawn², Peter Thorne³, and Andrew Parnell⁴

¹Dipartimento di Scienze Ambientali, Informatica e Statistica, Università Ca' Foscari, Venezia, Italia. daire.healy@unive.it

²Department of Mathematics and Statistics, Lancaster University, Lancaster, UK.

³Irish Climate Analysis and Research UnitS (ICARUS), Department of Geography, Maynooth University, Maynooth, Ireland.

⁴School of Mathematics and Statistics, University College Dublin, Dublin, Ireland.

Abstract

We analyse extreme daily minimum temperatures in winter months over the island of Ireland from 1950–2022. We model the marginal distributions of extreme winter minima using a generalised Pareto distribution (GPD), capturing temporal and spatial non-stationarities in the parameters of the GPD. We investigate two independent temporal non-stationarities in extreme winter minima. We model the long-term trend in magnitude of extreme winter minima as well as short-term, large fluctuations in magnitude caused by anomalous behaviour of the jet stream. We measure magnitudes of spatial events with a carefully chosen risk function and fit an r -Pareto process to extreme events exceeding a high-risk threshold. Our analysis is based on synoptic data observations courtesy of Met Éireann and the Met Office. We show that the frequency of extreme cold winter events is decreasing over the study period. The magnitude of extreme winter events is also decreasing, indicating that winters are warming, and apparently warming at a faster rate than extreme summer temperatures. We also show that extremely cold winter temperatures are warming at a faster rate than non-extreme winter temperatures. We find that a climate model output previously shown to be informative as a covariate for modelling extremely warm summer temperatures is less effective as a covariate for extremely cold winter temperatures. However, we show that the climate model is useful for informing a non-extreme temperature model.

Keywords: Climate change, extreme winter temperatures, spatial extremes, generalised Pareto distribution, r -Pareto processes

1 Introduction

The frequency and intensity of extremely cold temperatures have decreased globally since 1950 with this trend expected to continue as global mean temperatures rise (IPCC, 2021, Chapter 11). Winter temperatures have been particularly warming in the northern mid-latitudes (Matthes et al. 2015, Oldenborgh et al. 2019). In Ireland, significant warming of minimum air temperatures has been observed with decreasing frequency of cold events over the period 1885–2018 and are in line with global trends (Nolan and Flanagan, 2020, Mateus and Coonan, 2022, García et al., 2022). Extreme minimum temperatures are increasing faster than maxima, both globally (Dunn et al., 2020) and in Ireland, where the rate of change of temperature minima is twice that of maxima over the period 1950–2003 (McElwain and Sweeney, 2003).

Extremely high temperatures receive a substantially disproportionate amount of analysis in the literature given their direct and immediate link to loss of life (Ballester et al., 2023), crop failure

(He et al., 2022), etc. Furthermore, the intensity, duration and extent of heatwaves are expected to increase with global temperatures (Perkins-Kirkpatrick and Lewis, 2020), exacerbating impacts and demanding immediate attention. While the warming of winter temperatures is less immediately disruptive, it nonetheless harbours many potentially devastating consequences. Changes in winter extremes are having an effect on many facets of our environment and society, from mortality and morbidity rates (Conlon et al., 2011), to agricultural activity (Bindi and Olesen, 2011; Hooker et al., 2008) and ecosystems (Osland et al., 2021). For example, many regions rely on cold winters to control pathogens and pest populations (Skendžić et al., 2021). It has been argued that the consequences of warming winters have been understudied (Boucek et al., 2016).

Irish winters are generally less severe compared to many countries at similar latitudes due to the regulating effect of the North Atlantic Ocean and the Irish Sea surrounding the island. The winter of 2019 was the warmest on record for Ireland at 0.9°C above the 1961–1990 average winter temperature (Met Éireann, 2019). However, in northern Europe, warming trends are contrasted with occasional, extreme cold events associated with variability in climatic oscillations, i.e., Arctic Oscillation (AO) and the North Atlantic Oscillation (NAO) (Vihma et al., 2020). The coldest temperatures in some parts of Ireland were observed as recently as 2010, for example, a record low of -17.5°C was observed in Co. Mayo, Straide (Christiansen et al., 2018). The extremely cold winter of 2009/10 was caused by an anomalously persistent negative phase of the North Atlantic Oscillation (Cattiaux et al., 2010). A similar event occurred in the winter of 1962/63, where a Scandinavian anticyclone, marked by a negative phase of the North Atlantic Oscillation, brought easterly winds over Ireland resulting in extremely cold temperatures (Sippel et al., 2024). Throughout the analysis, we highlight the winter of 2009/10 as the primary example of an unusually cold winter event given its more recent occurrence and its more abundant data availability.

Figure 1 shows that globally (left-hand plot), the winter months of December, January, and February (DJF) of 2010 were anomalously warm, despite large variations locally, for example in Ireland (right-hand plot). Disentangling these juxtaposing trends in winter extremes is important to fully ascertain the overall trend of winter extreme temperatures. Christiansen et al. (2018) show that the cold winter of 2009/10 was in fact warmer than expected, in the context of the climate conditions at the time. The authors estimate that the occurrence probability of extremely cold winter temperatures such as those seen in 2009/10 has reduced by a factor of 2 due to anthropogenic-induced climate change, and so were in line with global warming winter trends.

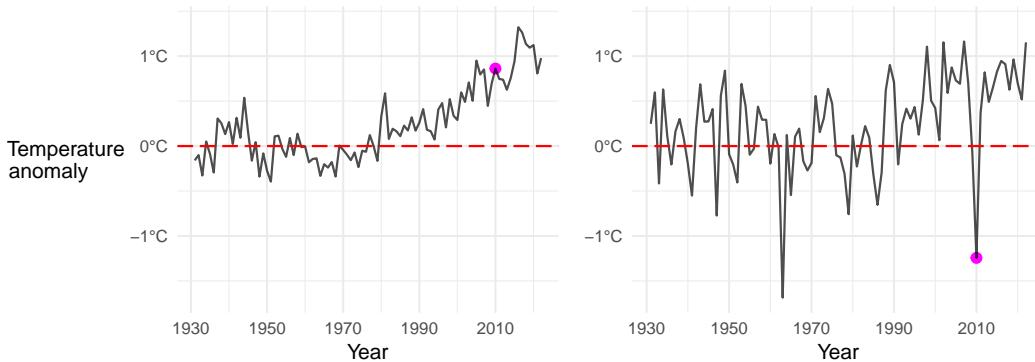


Figure 1: Global (left) and Irish (right) mean winter (DJF) temperature anomalies with 2010 highlighted. Calculated from HadCRUT5. Anomalies are relative to a 1961–1990 reference period.

Our analysis aims to test for and identify non-stationarities in winter temperature extremes to give a more thorough picture of the impact of climate change on winter temperatures in Ireland. To avoid underestimating the severity of extreme weather events, we rely on asymptotically justified statistical

models provided by extreme value theory. Advances in the extreme value literature enable us to model the spatial dependence of extreme observations, which allows the simulation of spatial extreme winter temperature events. We use the generalised r -Pareto process (Dombry and Ribatet, 2015) to model extremal dependence since this approach involves fitting the model to full spatial observations. The r -Pareto process more accurately captures realistic spatial patterns of extreme events as opposed to the max-stable process, which models constructed componentwise maxima, typically not corresponding to actual observed spatial events.

Our main contributions include adapting the methodology of Healy et al. (2024) in order to account for high levels of autocorrelation within cold temperature extremes and the high variability of extreme temperatures governed by external large-scale short-term climatic patterns. To achieve this, we develop a novel bootstrapping method which accounts for strong temporal dependence and complex variability in winter extremes, providing more accurate uncertainty estimates in our modelling. We identify non-stationarities in extremely cold winter temperatures in Ireland, considering larger-scale atmospheric patterns in which they occur. Our approaches incorporate such as the NAO and AO, together with the HadCRUT5 dataset and Regional Climate Model output, to represent the climatic processes driving these extremes. We assess the marginal and dependence structures of extreme winter events and provide a comprehensive analysis of the spatial risk over time. Our analysis underlines the importance of considering short-term climatic variability when modelling extreme weather processes, for which we propose a novel framework.

Our paper is organised as follows. Section 2 details the observational and climate model data used as well as additional covariates explored. Section 3 and Section 4 describe the marginal and dependence modelling of the process respectively. In Section 5, we use the model to explore how the properties of spatial extreme events have changed over time. Conclusions and a broader discussion are given in Section 6. All our code and instructions on how to access the data are available on GitHub¹.

2 Data

Modelling extreme minima of a series of *iid* observations is practically equivalent to modelling extreme maxima. For our analysis, we apply an inverse transformation to our series of minimum daily temperatures and analyse them as maxima, that is, we apply the transformation

$$\min(X) = -\max(-X). \tag{1}$$

Finally, we report all results on the original scale, after applying the inverse of (1). For ease of interpretation, we discuss temperatures on the original scale throughout. We use several data sources to achieve a full spatial and temporally non-stationary model of extremely cold winter temperatures. These data sources are discussed below.

2.1 Station data

For the purpose of this study, we focus on modelling the extremal behaviour of observational temperature data. We consider observed temperature data to avoid pre-processed data products which may influence or smooth out extremal behaviour (Donat et al., 2014). The creation of data products may involve omitting some extreme values mistakenly identified as outliers and smoothing spatial patterns which can have a great impact on the magnitude of unusually large or small events.

Our daily minimum temperature data comprise Irish temperature stations compiled from two sources, with observational data for the Republic of Ireland provided by Met Éireann’s data archive², while Northern Ireland sites were obtained through the Met Office Integrated Data Archive System (MIDAS; Met Office, 2012). The data exhibits a substantial amount of missingness, with data availability greatly decreasing as we go back in time. Although we have some data prior to 1950, for the

¹<https://github.com/dairer/Extreme-Irish-Winter-Temperatures>.

²Copyright Met Éireann. <https://www.met.ie/climate/available-data/historical-data>.

purpose of comparing different climatic covariates (discussed in Section 2.3.1), which are only available mutually since 1950, we restrict our analysis to data from the period 1950–2022. The data set contains some outliers that were not physically realistic, we took a conservative approach to remove these values to avoid discarding any true, extreme observations. Thus, we only removed any temperatures that were greater than 4 (empirically estimated) standard deviations away from the mean minimum temperature on a given day. This procedure removed 93 unrealistic observations from the data set. Keeping sites that had at least 5 years of data, we have a collection of 125 sites with a total number of approximately 330,000 daily minimum winter (December, January, February; DJF) temperature records over Ireland.

Our interest is in extreme cold temperatures in Ireland, so we restrict our analysis to data from the winter months (DJF). In Figure 2, we look at the number of exceedances per month when we take high site-wise quantiles as thresholds. The majority of extreme cold events occur in the winter months December, January, and February. Specifically, we find that more than 80% of all the days with temperatures below the 1% site-wise marginal quantile occur in DJF. However, there is a non-negligible number of extreme events in March (12% of events below the site-wise 1% quantile). We initially modelled the winter months (DJF) including March in our analysis, however, we found that the weather processes governing extremely low temperatures in the month of March were not captured well by our modelling procedure. The inclusion of March requires careful modelling of seasonality which is beyond the scope of this work and so we leave this as future research. We thus model only the winter months (DJF) which contain the majority of temperature extremes.

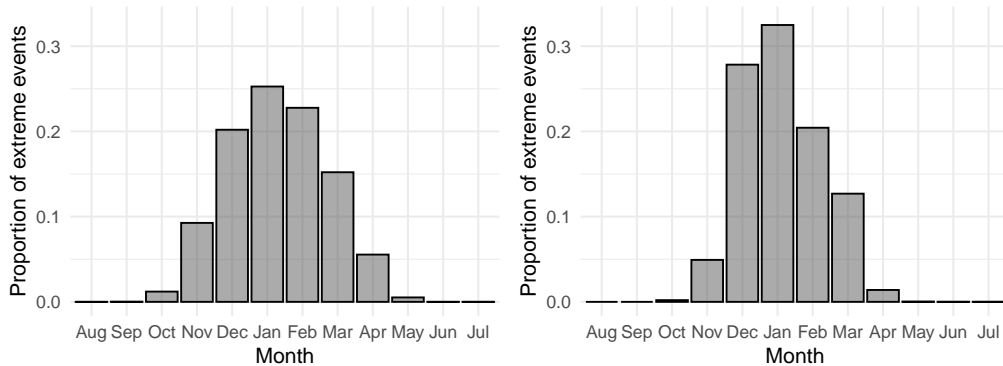


Figure 2: Proportion of threshold exceedances per month where the threshold corresponds to 5th (left) and 1st (right) site-wise percentile.

2.2 Spatial covariates

2.2.1 Climate model output

We explore the efficacy of exploiting physical information from climate model outputs as a spatial covariate. Climate models are mathematical representations of the physical processes driving weather and climate and represent our best understanding of these natural phenomena (Giorgi, 2019). They are computationally expensive, and so to model the climate on a fine scale requires limiting ourselves to specific regions. Climate models are broadly run on two scales, global climate models (GCMs) and regional climate models (RCMs). We use the output from RCMs to incorporate more detailed descriptions of the physics and spatial characteristics into the modelling of temperature extremes. We take data from the CLMcom-CLM-CCLM4-8-17 RCM (see Figure 3) combined with the ICHEC-EC-EARTH GCM (Service, 2019). From the models, we have daily minimum temperature values over a 56-year period, on a regular grid of 558 points over Ireland (corresponding to a 0.11^2 degree resolution). For a given ensemble we are required to select a so-called “experimental configuration”.

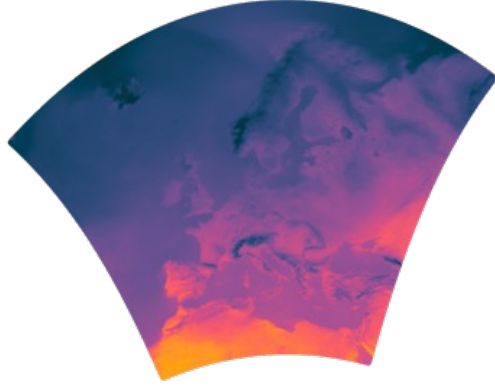


Figure 3: Full spatial extent of the RCM CLMcom-CLM-CCLM4-8-17, showing a generated temperature event for a randomly chosen day.

Historical experiments are climate simulations for a period in which observational data exists, but they fundamentally differ from reanalysis data as they are not designed to match day-to-day weather observations, focusing instead on capturing general weather processes. For our chosen ensemble this period covers 1951–2005. To simulate data beyond this period it is necessary to make some assumptions about future climate change. However, our analysis does not require climate model output for informing temporal non-stationarity so we rely solely on the historical experiment for our spatial analysis. We do not use the climate model output as a direct covariate, rather, we first fit an extreme value model to the climate model output and use the parameter estimates as covariates in our final model of the observed data, technical detail on this procedure is given in Section 3.

2.2.2 Coastal distance

There is an evident difference in temperature levels between coastal and inland areas in Ireland, especially so in winter (Mateus and Coonan, 2022). This spatial effect is due to the strong influence of the Irish Sea and the Atlantic Ocean on Irish air temperatures. We are thus motivated to employ coastal proximity as a covariate to examine its efficacy in explaining the spatial distribution of cold extremes. We denote coastal proximity at site s as $C(s)$, calculated as the Euclidean distance from the nearest coastal point.

2.3 Long-term temporal trend covariate

For modelling the long-term temporal trend in winter extremes, we use temperature anomalies taken from the HadCRUT5 data set (Morice et al., 2021) as a temporal covariate to assess how extreme cold temperatures are changing with respect to mean temperature levels. Unlike the climate model output discussed in Section 2.2.1, HadCRUT5 incorporates observational data, combining temperature measurements with interpolated values to fill spatial gaps, rather than relying on simulated physics-based weather models. We perform LOESS smoothing on temperature anomalies during winter months over the grid point containing Ireland from the HadCRUT5 data set. We use the R language implementation of LOESS smoothing, taking the default span of 0.75 and degree of 2 (Team, 2023). We denote this smoothed temporal covariate as $M^I(t)$ and use it to account for the large-scale temporal trend in the data. The covariate $M^I(t)$ is plotted in Figure 4, illustrating an increase of approximately 0.9°C in mean winter temperature anomalies over the period 1950–2022.

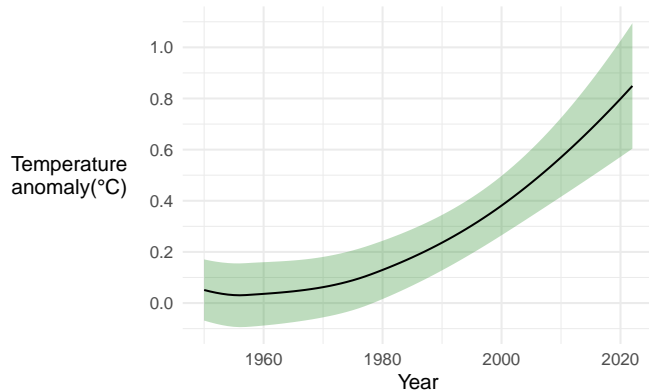


Figure 4: LOESS smoothed Irish winter temperature anomalies from HadCRUT5 with shaded regions showing 95% confidence intervals.

2.3.1 Climatic oscillation covariates

In our analysis, we aim to disentangle the general, long-term trend of extremely cold winter temperatures from the large variations caused by external, highly-variable, climatic processes. To this end, we explore numerous climatic variables to help explain extreme, sudden cold snaps, which can misleadingly be interpreted as contradicting warming winters.

It is well understood that the behaviour of the jet stream can lead to shifts in weather patterns, including the occurrence of extreme events such as cold spells (Stendel et al., 2021). The jet stream is a high-altitude, fast-flowing air current that circumvents the northern hemisphere in the upper troposphere and lower stratosphere. The jet stream plays a crucial role in shaping weather patterns and controlling the movement of storms and weather systems (Hoskins and James, 2014). The jet stream meanders in a wave-like pattern as it circumnavigates the globe. These waves form and change in response to several climatic conditions and are characterised by northward or southward oscillations. When these waves become amplified, we see a greater north-south displacement of air masses, resulting in the transport of air masses from different latitudes. When a deep southward dip forms in the jet stream, it can allow cold air to spill southward from the polar regions into lower latitudes causing extremely cold temperatures (Thompson and Wallace, 2001; Francis and Vavrus, 2012).

There is a strong link between the behaviour of the jet stream and extratropical teleconnections such as the North Atlantic Oscillation (NAO) and Arctic Oscillation (AO) (Hall et al., 2015). Both the NAO and AO have the greatest variability in winter months (Gupta and McNeil, 2012) which is when they have a substantial influence on weather patterns in the northern hemisphere (Thompson and Wallace, 1998). Furthermore, persistent and strong negative phases of the AO and the NAO have been linked with extremely low minimum air temperatures in Ireland (Mateus and Coonan, 2022). Thus, we are motivated to consider the efficacy of using NAO or AO as a covariate for anomalous jet stream behaviour and subsequently extreme cold winter temperatures in Ireland.

The NAO is a climatic phenomenon that describes the state of the atmospheric pressure difference between the Icelandic Low and the Azores High in the North Atlantic. The NAO is known to influence the behaviour and position of the jet stream (Gerber and Vallis, 2009). In the positive phase, the pressure difference between the Icelandic Low and the Azores High is stronger than average. The stronger pressure difference confines the jet stream to higher altitudes, with a steady eastward flow. Conversely, during the negative phase of the NAO, the pressure difference weakens, allowing for a more meandering and meridional path of the jet stream. This allows the jet stream to dip southwards, pouring cold air masses onto northern Europe, leading to extremely cold temperatures. As a result, the jet stream may meander or become more amplified. A wavier jet stream generally leads to slower progression of weather systems, and subsequently more persistent weather regimes, such as persistent

cold air in a cold spell (Sousa et al., 2018). The NAO can be interpreted as the North Atlantic sector manifestation of the AO (IPCC, 2021, Annex IV: Modes of Variability) and so, the two variables are highly correlated.

The AO characterises changes in atmospheric pressure over the Arctic region (Thompson and Wallace, 1998). Analogous to the NAO, during the positive phase of the AO, the pressure difference between the Arctic and mid-latitudes is weaker and the jet stream is confined to higher latitudes. This means that weather systems and air masses tend to move more smoothly and quickly across the mid-latitudes (Deser, 2000). Conversely, during the negative phase of the AO, the pressure difference between the Arctic and mid-latitudes increases with elevated air pressure over the Arctic region and lower air pressure over the northern Pacific and Atlantic Oceans. Lower air pressure over the northern Pacific and Atlantic Oceans allows for an amplified meandering of the jet stream with a higher probability of extremely cold, polar air outbreaks in the mid-latitudes during winters.

We retrieve data for the NAO and AO from the National Weather Service, Climate Prediction Center³, taking monthly and yearly mean AO and NAO values from 1950 onwards. The climatic oscillation covariates are shown in Figure 5. Notice that in both plots, we see a large deviation from the mean around the year 2009/10, which appears more pronounced in the AO series.

NAO and AO indices are not a perfect proxy for the behaviour of the jet stream. Other atmospheric and oceanic patterns, such as high-pressure systems and sea surface temperatures, can also interact with the jet stream and influence the occurrence of cold weather events (Screen and Simmonds, 2014). Overall, the interaction between the jet stream, atmospheric, and oceanic patterns is a complex and dynamic process (Hall et al., 2015). The interplay of these factors can lead to changes in the jet stream’s behaviour, which in turn affects weather patterns, including the occurrence of cold spells (Kidston et al., 2015).

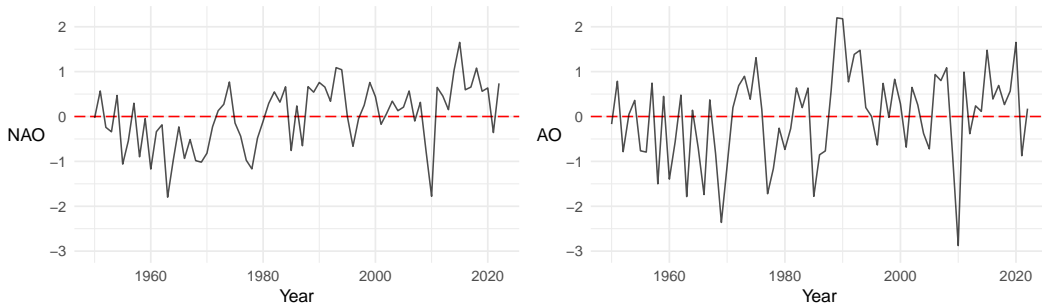


Figure 5: Yearly North Atlantic Oscillation (NAO) index over the period 1950–2022 (left). Yearly Arctic Oscillation (AO) index over the period 1950–2022 (right).

2.4 Short-term temporal trend covariate

Throughout the analysis we investigate the effect of monthly covariates; these will be indicated by a subscript m . Covariates without subscript m can be assumed to be yearly. The HadCRUT5 data set which we use to derive our long-term temporal covariate (see Section 2.3) seems an attractive candidate to describe the larger-scale processes governing cold temperatures since HadCRUT5 is an observation-based data product of temperatures produced as a combination of a land temperature anomaly data set (CRUTEM5; Osborn et al., 2021) merged with a sea-surface temperature anomaly data set (HadSST4; Kennedy et al., 2019). An appealing feature of this procedure is that it accounts for and encapsulates the effects of all climate processes that affect temperature, e.g., including the NAO and AO, and therefore the behaviour of the jet stream. We wish to capture large temperature deviations which are encoded in the HadCRUT5 data set. We use the residuals from the LOESS

³Available at: <https://www.cpc.ncep.noaa.gov>.

smoothing (see Section 2.3) as a covariate to explain the effect of large-scale climatic oscillatory patterns on winter extremes. In this way, we construct two independent covariates from the HadCRUT5 data set. We calculate the residual temperature anomalies by subtracting the observed temperatures from the smoothed temperature trend $M^I(t)$, and so positive residual values correspond to anomalously cold temperatures not captured by $M^I(t)$. We explore the efficacy of taking residuals from the LOESS smoothing of temperature anomalies during winter months ($M^I(t)$) on a monthly (denoted $M_{r,m}^I(t)$) and yearly averaged (denoted $M_r^I(t)$) basis, both of which can be seen in Figure 6. Notice in these time series, the large positive deviation around the year 2009/10, as the LOESS smoothing under-represents these extremely cold winters. This deviation corresponds to a large, negative temperature anomaly over Ireland described in the HadCRUT5 data set.

Furthermore, we explore the efficacy of using temperature residuals from grid boxes surrounding Ireland, $M_r^G(t)$, as well as the grid box directly above Ireland, $M_r^N(t)$, after removing the smoothed temperature $M^I(t)$ trend. Both time series as well as their associated HadCRUT5 grid box(es) can be seen in Figure 7. In both time series, we can see large deviations in mean temperatures, for example in the year 2009/10.

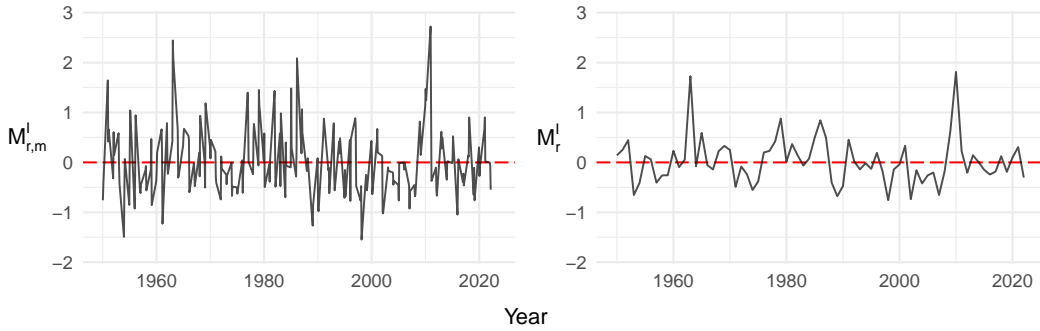


Figure 6: Residuals from HadCRUT5 temperature values over Ireland after LOESS smoothing (left). Average yearly residuals from HadCRUT5 winter temperature values over Ireland after LOESS smoothing (right).

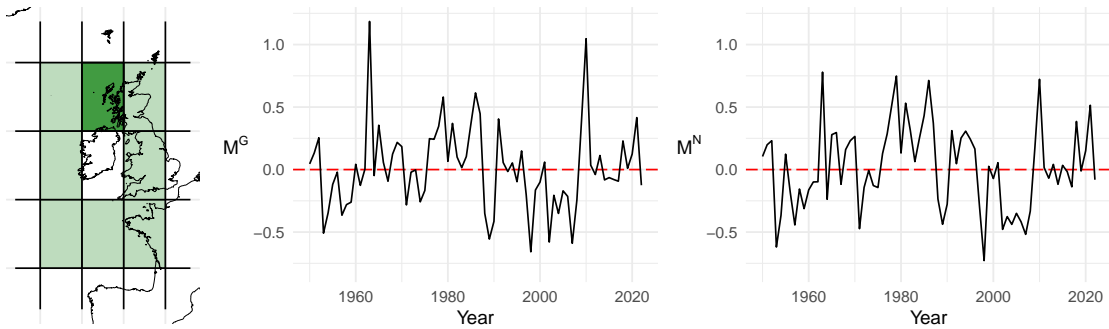


Figure 7: Illustration of gridding of the HadCRUT5 data set over northwest Europe centred on Ireland, with grid boxes surrounding Ireland lightly shaded and the grid box north of Ireland heavily shaded (left). Time series of residual yearly temperature anomalies averaged from all shaded grid boxes surrounding Ireland (centre) and from grid box north of Ireland (right).

3 Marginal models

3.1 Overview and strategy

Let $X_o(t, \mathbf{s})$ denote the observed minimum daily temperature at time t and site \mathbf{s} during winter months, and let $X_c(t, \mathbf{s})$ be the minimum daily temperature from the climate model at time t and site \mathbf{s} . The subscripts o and c are used throughout, referring to observation and climate model processes respectively, the subscripts are dropped when discussing methods mutual to both. Here $t \in \mathbb{N}$ indexes winter days within and across years and $\mathbf{s} \in \mathcal{S} \subset \mathbb{R}^2$, where \mathcal{S} denotes the island of Ireland, with \mathbf{s} corresponding to the vector of latitude and longitude. We have data on the two processes at $\mathcal{S}_o \subset \mathcal{S}$ and $\mathcal{S}_c \subset \mathcal{S}$ and at times \mathcal{T}_o and \mathcal{T}_c respectively.

For modelling $X_o(t, \mathbf{s})$, we account separately for the behaviour of the non-extremal temperatures below the threshold $u_o(\mathbf{s})$, denoted as the *bulk* model and the extremal temperatures above, denoted as the *tail* model. In Section 3.3.1, we use interpolated quantiles estimated via spatial quantile regression to model the data below the threshold. We also derive our estimate of the threshold and threshold exceedance parameter in Section 3.3.3, allowing for a smooth and continuous transition from the bulk to the tail model. In Section 3.3.4, we present the parameterisations of the generalised Pareto distribution we explored, which model the extreme temperatures above the threshold. Throughout, we derive spatial covariates from the climate model output $X_c(t, \mathbf{s})$ to inform each of our modelling stages. We discuss the efficacy of using the climate model output to inform the spatial behaviour of extreme winter temperatures. In Section 3.3.6, we detail a novel, relaxed bootstrapping algorithm that deals with highly auto-correlated extremal data with substantial missing data.

3.2 Cross-validation

For characterising marginal model fit performance and model selection, we use cross-validation (Hastie et al., 2009, Ch 7.). We use both standard n -fold CV (n -CV) and spatio-temporal CV (ST-CV). For ST-CV, observational sites are divided spatially into 15 contiguous groups and 3 temporal folds. Each temporal fold consists of every third week in the winter months in order to preserve long-term temporal non-stationarity. We define 45 ST-CV folds as all combinations of spatial and temporal clusters, taking the intersection as a fold. For n -CV the data are divided into 45 groups (folds) to correspond to the number of spatio-temporal folds. For both ST-CV and n -CV, we iteratively excluded one fold from the data set and fit the model to the remaining data. We test the model’s predictive ability on the out-of-sample data using the root mean square error (RMSE) and the continuous ranked probability score (CRPS, Gneiting and Katzfuss, 2014). This process is repeated for each fold, with final performance metrics averaged across folds.

3.3 Marginal data analysis

3.3.1 A model for the body of the distribution

To estimate the distribution function of $X_o(t, \mathbf{s})$, we use the asymmetric Laplacian distribution (ALD) for quantile regression. We estimate a range of spatially and temporally varying τ th quantiles of $X_o(t, \mathbf{s})$ (denoted as $q_o^{(\tau)}(t, \mathbf{s})$) for a grid of $\tau \in \{0.01, 0.02, \dots, 0.99\}$, for all $t \in \mathcal{T}$ and $\mathbf{s} \in \mathcal{S}$. Following this, we use a cubic interpolation spline for each t and \mathbf{s} to give a continuous estimate over τ .

We explored several potential parameterisations for the ALD, which we present in Table 1, along with their cross-validation metrics (calculated as in Section 3.2). The first model in Table 1, *a.*, can be considered as the base model where a constant quantile is estimated over space and time for each τ . The second model, *b.*, includes the smoothed temperature anomalies over Ireland, $M^I(t)$, as a covariate to allow for temporal non-stationarity in the model of the body of the distribution. The third model, *c.*, allows the quantile estimates to vary spatially using the corresponding climate model output quantiles, $q_c^{(\tau)}(\mathbf{s})$ as a covariate. The fourth model *d.* combines the coefficients of models *b.* and *c.*, allowing for both spatial and temporal non-stationarity.

We found the performance of the model greatly improved when incorporating a coastal proximity covariate $C(\mathbf{s})$. This is shown in the reduction of RMSE values achieved by model e . over d . in Table 1. We found a further substantial improvement in RMSE with the inclusion of a covariate to account for unusually cold weather events caused by large-scale climate oscillation. We chose the covariate that was best performing in the tail model (discussed in detail in Section 3.3.4) for the sake of parsimony, continuity, and interpretability of the *bulk-to-tail* model. That is, we use the residuals from the LOESS smoothing of temperature anomalies during winter months, $M_{r,m}^I(t)$ as a covariate in the bulk model. We use bulk model f . for the remainder of the analysis.

Table 1: Cross-validation (RMSE) on the quantile regression analysis for the body of the distribution.

Model structure for $\hat{q}_0^{(\tau)}(t, \mathbf{s})$	ST-CV	n-CV
a. $\beta_0^{(\tau)}$	2.019	2.028
b. $\beta_0^{(\tau)} + \beta_1^{(\tau)} M^I(t)$	1.991	2.028
c. $\beta_0^{(\tau)} + \beta_1^{(\tau)} q_c^{(\tau)}(\mathbf{s})$	1.898	1.912
d. $\beta_0^{(\tau)} + \beta_1^{(\tau)} q_c^{(\tau)}(\mathbf{s}) + \beta_2^{(\tau)} M^I(t)$	1.864	1.891
e. $\beta_0^{(\tau)} + \beta_1^{(\tau)} q_c^{(\tau)}(\mathbf{s}) + \beta_2^{(\tau)} M^I(t) + \beta_3^{(\tau)} C(\mathbf{s})$	1.764	1.756
f. $\beta_0^{(\tau)} + \beta_1^{(\tau)} q_c^{(\tau)}(\mathbf{s}) + \beta_2^{(\tau)} M^I(t) + \beta_3^{(\tau)} C(\mathbf{s}) + \beta_4^{(\tau)} M_{r,m}^I(t)$	1.218	1.221

The coefficients of model f . are shown in Figure 8 along with 95% uncertainty intervals based on 200 spatio-temporal bootstrap samples, described later in Section 3.3.6. Since we are modelling negated temperatures, higher quantiles correspond to colder temperatures. The estimates of $\beta_1^{(\tau)}$ show that the climate model does not provide a perfect description of the station data, as the estimates differ from 1 significantly and change with τ . This suggests that the chosen climate model output is not sufficient in and of itself in representing daily winter minima. However, the climate model is still informative here, especially at quantiles near the center of the data ($0.4 < \tau < 0.6$), where it is significantly different from zero. However, the climate model covariate appears to become less informative towards the extremes of the process as we see the effect of the q_c^τ falling off at both tails of the distribution ($\tau < 0.2$ and $\tau > 0.8$). For the majority of the body of the distribution, we see that $\beta_2^{(\tau)} \approx -1$. This indicates that mean winter temperatures in Ireland are a good representation of the temporal change for the majority of the body of the distribution. However, we see the effect of $M^I(t)$ increasing at higher quantiles ($\tau > 0.75$), suggesting extremely cold daily winter temperatures events are changing faster than mean minimum daily winter temperatures. We see that the effect of coastal proximity increases almost linearly with quantiles τ , giving a sufficient spatial description of the process not provided by the climate model output. Finally, $\beta_4^{(\tau)}$ suggests, unsurprisingly, that large-scale oscillations are useful for explaining the most extreme cold events, for example, seen as the increase in the uppermost quantiles ($\tau > 0.75$).

3.3.2 Phases of short-term climate variability (SCV)

Since we use a highly-variable covariate, $M_{r,m}^I(t)$, in the bulk model parameterisation f . (and later in the tail model), every result derived using this covariate will be similarly highly variable and not smooth. For the sake of interpretability, we report results at three different quantile levels of the variable $M_{r,m}^I(t)$. That is, we present results associated with the 0.1, 0.5 and 0.9 quantiles of the covariate $M_{r,m}^I(t)$, and denote these levels as $M_{r,m}^{(\tau),I}(t)$ where $\tau \in \{0.1, 0.5, 0.9\}$. Throughout this analysis, we will refer to these as low, median, and high phases of short-term climate variability (SCV) respectively. Reporting results associated with quantiles of the covariate alleviates any findings associated with the variability of any specific covariate. Instead, this method provides a general interpretation of different levels of extremity in the context of different phases of large-scale climatic processes. Note that the high phase of SCV, $M_{r,m}^{(0.9),I}(t)$, corresponds to a large negative phase of NAO

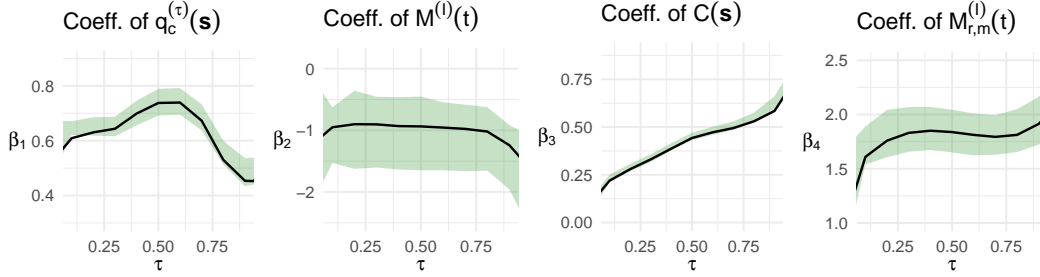


Figure 8: Estimates of bulk model f . coefficients $\beta_1^{(\tau)}$, $\beta_2^{(\tau)}$, $\beta_3^{(\tau)}$, and $\beta_4^{(\tau)}$ of $q_c^{(\tau)}(\mathbf{s})$ (corresponding climate output quantile), $M^I(t)$ (smoothed temperature anomalies over Ireland), $C(\mathbf{s})$ (coastal distance), and $M_{r,m}^I(t)$ (monthly residuals of $M^I(t)$) respectively over a range of quantiles τ . In each case, the shaded region indicates bootstrap-based pointwise 95% confidence intervals. Higher quantiles correspond to colder temperatures.

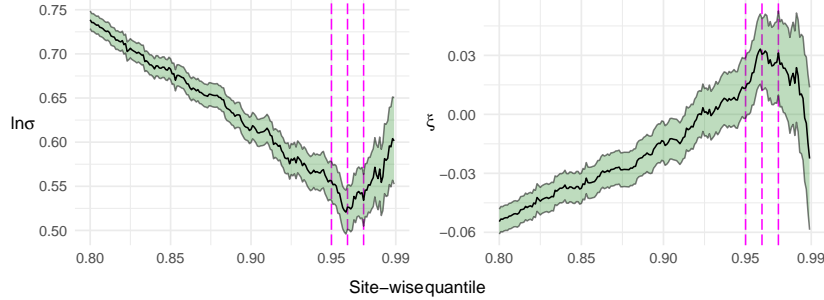


Figure 9: Parameter stability plot of the GPD parameters, σ and ξ over a range of quantiles used to calculate a site-wise threshold. Three vertical dashed lines represent the 0.95, 0.96, and 0.97 quantiles. The shape parameter, ξ , appears to stabilise around the 0.96 quantile.

and AO and subsequently a pronounced meandering of the jet stream which we know is linked to more extreme cold spells in Northern Europe, as well as Ireland (as discussed in Section 2.3.1)

3.3.3 Threshold selection

For threshold selection, we examine the stability of the parameters of the generalised Pareto distribution over a range of thresholds as shown in Figure 9. For a sequence of 200 quantiles, between 0.8 and 0.999 we empirically estimate the temperature at that quantile for each site (\mathbf{s}) separately. We treat this quantile as a threshold and fit a generalised Pareto distribution to the excesses above each threshold, pooled over space. The estimates of the generalised Pareto distribution parameters $\ln \sigma$ and ξ are plotted, along with associated 95% confidence intervals for each quantile. Since the generalised Pareto has a threshold stability property (Davison and Smith, 1990), we know that once a sufficiently high threshold is chosen, the exceedance of any higher threshold will be similarly generalised Pareto distributed with the same shape parameter and a deterministic shift in the scale parameter. In Figure 9, we can see this appears to happen around the 0.96 quantile.

The winter of 2009/10 represents a disproportionately large percentage of extreme events. We have over 73 years of data, with almost 17% of extreme observations occurring in the winter of 2009/10, while, on average, each year has 1.36% of all extreme events. It is clear the behaviour of extremes is different in 2009/10 from those in other years. For example, the temperature at the 0.9 quantile of minimum daily temperatures in 2009/10 is approximately twice as cold (in the Celsius scale) as the average yearly temperature at the 0.9 quantile. This anomalous period certainly has a substantial impact on the tail of the entire data distribution. Despite this, extreme observations above the 0.96

quantile of temperatures are evenly spread across space and time, with the exception of the winter 2009/10. Even at this high threshold, we believe we have sufficient extreme observations to achieve our modelling goal of allowing the scale parameter to capture the long-term non-stationarity in a parsimonious manner.

To alleviate the impact of the winter of 2009/10 on the estimation of the threshold, we could use a different threshold estimate during 2009/10 from other years. However, a step function at the threshold greatly reduces the interpretability and parsimony of our model. Instead, we rely on more physically interpretable covariates (described in Section 3.3.2, such as $M_{r,m}^I(t)$) which capture SCV, and directly reflect the unusual behaviour of the especially extreme behaviour 2009/10. We could incorporate this covariate into our threshold estimation. It is a non-trivial choice as to whether to deal with this complex non-stationarity in the threshold or in the parameters of the GPD tail model. Since we have data evenly spread across all periods above our high threshold and to preserve the parsimony of the model, we choose to keep a temporally constant threshold, and account for the highly variable behaviour in the temperature process by incorporating the SCV covariate into the scale parameter of the GPD.

To ascertain the sensitivity of this choice, we perform analysis based on the three quantiles marked as vertical lines in Figure 9, i.e., we use the 0.95, 0.96, and 0.97 quantiles as thresholds. Our primary analysis is performed using the 0.96 quantile, however, we calculate results at all three quantiles to establish threshold selection sensitivity.

To estimate the threshold, we perform spatial quantile regression using the ALD as detailed in Section 3.3.1. The threshold is estimated as,

$$u_o^{(\tau)}(\mathbf{s}) = \beta_0^{(\tau)} + \beta_1^{(\tau)}q_c(\mathbf{s}) + \beta_2^{(\tau)}C(\mathbf{s}), \quad (2)$$

where $\tau = 0.95, 0.96$, or 0.97 . Note that our model of $u_o^{(\tau)}(\mathbf{s})$ is equivalent to the model formulation of models *e.* and *f.*, in Table 1 without temporal non-stationarity. Estimates of $u_o^{(\tau)}(\mathbf{s})$ using (2) for each $\tau \in \{0.95, 0.96, 0.97\}$ can be seen in Figure 10, where columns left to right correspond to increasing values of τ . Figure 10 shows that inland areas of Ireland experience cooler winter temperatures.

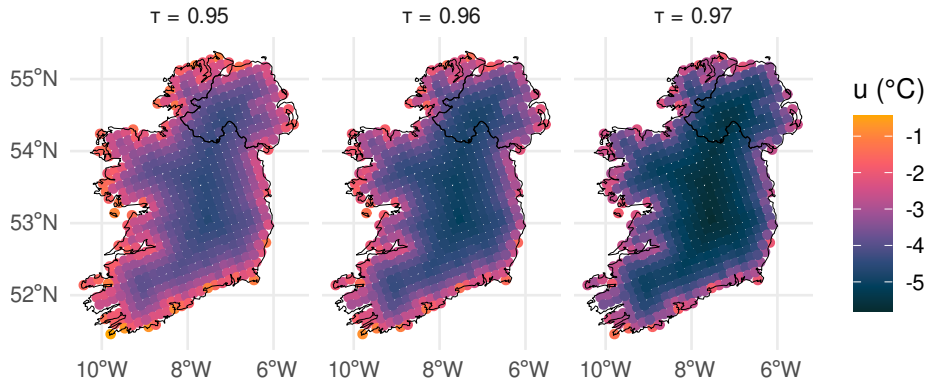


Figure 10: Estimates of threshold $u_o^{(\tau)}(\mathbf{s})$ with values of $\tau = 0.95, 0.96, 0.97$ from left to right.

In Figure 11, we calculate estimates of the threshold exceedance probability, λ , associated with low, median, and high phases of SCV and present its spatial average $\lambda_o(t) = \int_{\mathbf{s} \in \mathcal{S}_o} \lambda_o(t, \mathbf{s}) d\mathbf{s} / |\mathcal{S}_o|$. The presented estimates of $\lambda_o(t)$ show a decreasing exceedance rate over the period 1950–2022, for each phase of SCV (low to high from left to right). For the median phase of SCV, i.e., $M_{r,m}^{(0.5),I}(t)$, in the centre plot, the threshold exceedance rate over time of 0.04 – 0.015 reflects the choice of the threshold

as 0.96. During the low phase of SCV, i.e., $M_{r,m}^{(0.1),I}(t)$, in the left-hand plot, we have much smaller threshold exceedance probabilities, indicating a much lower occurrence rate of extremely cold winter temperatures. In stark contrast, during the high phase of SCV, i.e., $M_{r,m}^{(0.9),I}(t)$, in the right-hand plot, we see a much higher occurrence of extremely cold winter temperatures.

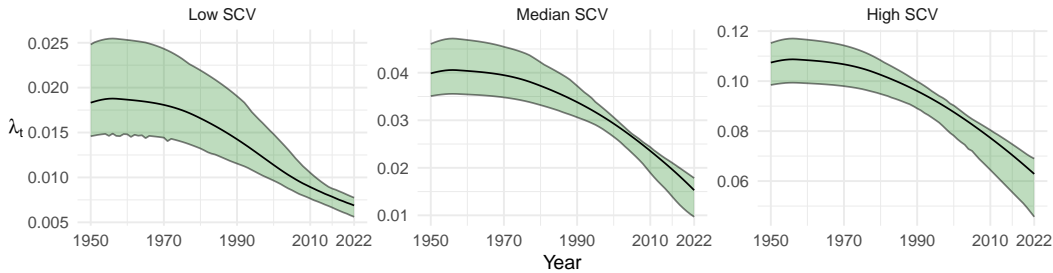


Figure 11: Threshold exceedance probability $\lambda_o(t)$ for t from 1950 to 2022 averaged over \mathcal{S} , corresponding to low (left), median (centre) and high phases (right) of SCV. In each case, the shaded region indicates bootstrap-based pointwise 96% confidence intervals.

3.3.4 Tail model

For each site $\mathbf{s} \in \mathcal{S}$, we assume that excesses of the threshold $u(\mathbf{s})$ follow a generalised Pareto distribution (GPD), with distribution function

$$H(y; \sigma, \xi) = 1 - (1 + \xi y / \sigma)_+^{-1/\xi} \quad (3)$$

for $y > 0$, with a shape parameter $\xi \in \mathbb{R}$ and a scale parameter $\sigma > 0$, with the notation $x_+ = \max(x, 0)$, and $\xi = 0$ is obtained by taking the limit as $\xi \rightarrow 0$. When $X(t, \mathbf{s}) > u(\mathbf{s})$ the threshold excess, $Y(t, \mathbf{s}) = X(t, \mathbf{s}) - u(\mathbf{s})$, is taken to be distributed as

$$Y(t, \mathbf{s}) \sim \text{GPD}(\sigma(t, \mathbf{s}), \xi). \quad (4)$$

We investigated numerous choices of models for $\sigma(t, \mathbf{s})$, broadly grouped into seven as presented in Table 2. In all models, we take the shape parameter to be constant over space and time for each model as is typical in non-stationary environmental applications of the GPD due to difficulty in estimating the parameter (Chavez-Demoulin and Davison, 2005). We perform a log-likelihood ratio test at each site to determine whether allowing the shape parameter to vary over space provides a significant improvement in the model fit. We take M_N , the null hypothesis, to be the model with constant shape parameter and M_A , the alternative, where each site has a different shape parameter estimate. For each site we compare the maximised pseudo-likelihood of M_N (i.e., $p\mathcal{L}\{M_N(\mathbf{s})\}$) and M_A , (i.e., $p\mathcal{L}\{M_A(\mathbf{s})\}$) and calculate the pseudo-likelihood ratio test statistic as $2 \ln [p\mathcal{L}\{M_A(\mathbf{s})\} / p\mathcal{L}\{M_N(\mathbf{s})\}]$. We found that over 91% of sites had a likelihood ratio below 0.05, with 95% of sites below 0.06. The total proportion of data in the sites with a test statistic greater than 0.05 is about 2.5% of extremal observations substantially below the standard likelihood ratio test statistic of 3.84. Furthermore, there was no clear spatial pattern in those sites with a test statistic higher than 0.05. Thus, we choose to keep a constant shape parameter.

As discussed in Section 1, extreme Irish winter minima are highly variable and strongly associated with large-scale climatic oscillations. We explore a set of potential covariates to explain the variability unaccounted for by $M^I(t)$. This extra covariate is denoted as $z(t)$ in Table 2.

The covariates $z(t)$ capture short-term climatic variability (SCV) and are detailed in Section 2.3.1. In each group in Table 2, $z(t)$ can also be the empty-set, \emptyset , so in each model group, we excluded the covariate $z(t)$ and explore the assumption that there is no climate variability unaccounted for by a

Group	Model structure for $\ln \sigma_o$
A	$\beta_0 + \beta_1 M^I(t) + \beta_2 z(t)$
B	$\beta_0 + \beta_1 \sigma_c(\mathbf{s}) + \beta_2 M^I(t) + \beta_3 z(t)$
C	$\beta_0 + \beta_1 \sigma_c(\mathbf{s}) + \beta_2 M^I(t) + \beta_3 C(\mathbf{s}) + \beta_4 z(t)$
D	$\beta_0 + \beta_1 \sigma_c(\mathbf{s}) + \beta_2 M^I(t) + \beta_3 M^I(t)C(\mathbf{s}) + \beta_4 z(t)$
E	$\beta_0 + \beta_1 C(\mathbf{s}) + \beta_2 M^I(t) + \beta_3 z(t)$
F	$\beta_0 + \beta_1 C(\mathbf{s}) + \beta_2 M^I(t) + \beta_3 M^I(t)C(\mathbf{s}) + \beta_3 z(t)$
G	$\beta_0 + \beta_1 M^I(t) + \beta_2 M^I(t)C(\mathbf{s}) + \beta_4 z(t)$
H	$\{\beta_0, \beta_0 + \beta_1 \sigma_c(\mathbf{s}), \beta_0 + \beta_1 C(\mathbf{s})\}$,

Table 2: GPD model groups. In each group, $z(t)$ represents all additional temporal covariates to capture short-term climatic variability. Model Group H is a set of 3 temporally stationary “base” models for comparison.

global trend. The set of covariates we present cross-validation results for is $z(t) = \{0, M_{r,m}^I(t), M_r^I(t), \text{NAO}(t), \text{NAO}_r(t), \text{NAO}_m(t), \text{NAO}_{r,m}(t), \text{AO}(t), \text{AO}_r(t), \text{AO}_m(t), \text{AO}_{r,m}(t), M_r^G(t), M_r^N(t)\}$, totalling 94 models which can be seen in Table 3. The covariates $\text{NAO}(t)$ and $\text{AO}(t)$, refer to the North Atlantic and Arctic oscillation values, respectively; $M_r^G(t)$ refers to the average HadCRUT5 values over the grid points surrounding Ireland, excluding the grid point over Ireland, and $M_r^N(t)$ refers to the average HadCRUT5 values over the grid points above Ireland. In each case, the subscript r refers to the residuals of that covariate after the trend of $M^I(t)$ is removed. A subscript m indicates monthly values, whereas no subscript m indicates that the average value over the winter months was taken for each year. We also investigated monthly values of $M_r^N(t)$ and $M_r^G(t)$. However, as compared to $M_r^I(t)$, their performance was generally worse in each case, so we do not include them for brevity. The spatial covariate $\sigma_c(\mathbf{s})$ represents the scale parameter of the GPD, fitted to $X_c(t, \mathbf{s})$, the climate model from the grid point closest to site \mathbf{s} . The covariate $\sigma_c(\mathbf{s})$ for each threshold $u_c^{(0.95)}(\mathbf{s}), u_c^{(0.96)}(\mathbf{s})$, and $u_c^{(0.97)}(\mathbf{s})$ estimated using climate model data is shown in Figure 12.

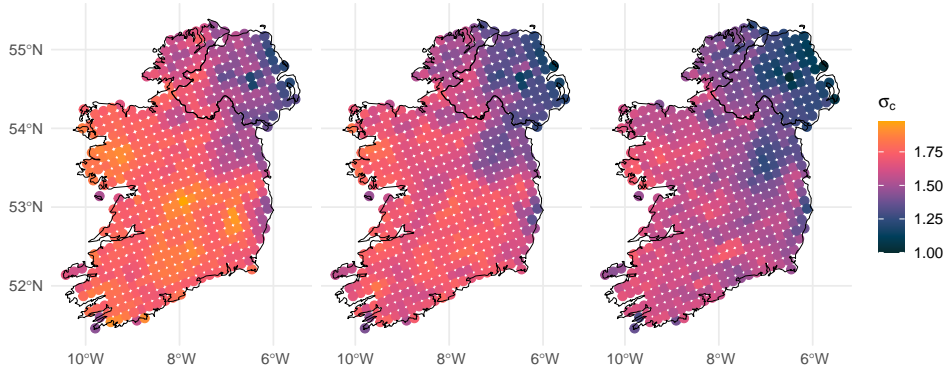


Figure 12: Climate scale covariate $\sigma_c(\mathbf{s})$ associated thresholds $u_c^{(0.95)}(\mathbf{s})$ (left), $u_c^{(0.96)}(\mathbf{s})$ (centre) and $u_c^{(0.97)}(\mathbf{s})$ (right) each with associated shape parameters $\xi = -0.12, -0.11$, and -0.09 respectively.

3.3.5 Model selection

In Table 2, Group A assumes spatial stationarity in the scale parameter. Groups B and C borrow spatial information from a climate model output, where C also explores a coastal proximity effect. Group D is equivalent to C but explores the interaction between the coast and long-term temporal

trends. Groups E and F do not borrow information from the climate model output, instead relying on coastal proximity to describe all spatial non-stationarity. Group G has no main spatial term, instead, it explores an interaction in space and time. We also consider “base” models in group H. Group H consists of three models, model H1 has no spatial or temporal non-stationarity. Model H2 incorporates $\sigma_c(\mathbf{s})$ as a spatial covariate and model H3 includes a coastal proximity covariate $C(\mathbf{s})$.

For the cross-validation metrics presented in Table 3, empirical quantiles used for calculating RMSE were estimated on yearly blocks of data for each site (in order to have sufficient data for estimating reasonable empirical quantiles, as well as preserving temporal non-stationarity). Therefore we do not report RMSE associated with models that have monthly non-stationary as their interpretation is not helpful. The CRPS does not require the specification of an observation quantile to assess the model performance. We thus use RMSE and CRPS jointly to identify the best-performing models and most effective covariates. Following this we use CRPS to choose whether to take a given covariate on a monthly or yearly scale.

The best models (highlighted in Table 3) all favour using HadCRUT5 residuals, $M_r^I(t)$, as a covariate for explaining SCV. This is unsurprising as all climatic forcings are encoded within HadCRUT5, and most informatively, their direct impact on temperature processes. The next most informative covariates $z(t)$ were $\{AO_r, NAO_r$ and, $M_r^G\}$. Furthermore, each of the best-performing models used coastal proximity as a covariate.

For base models in group H, we note that the inclusion of the climate-model-derived covariate $\sigma_c(\mathbf{s})$ yields no improvement over the spatially stationary model H1, suggesting the inefficacy of $\sigma_c(\mathbf{s})$ for informing the spatial nature of extreme cold temperatures. Surprisingly, the chosen climate model output is not as effective as a spatial covariate for modelling extremely cold winter events as it was found to be for extremely hot summer temperatures (Healy et al., 2024). However, the incorporation of the coastal proximity covariate $C(\mathbf{s})$, in model H3, achieves an improved CV score over the spatially stationary model H1.

In each pair of best-performing models, within each model group, CRPS prefers the monthly covariate $M_{r,m}^I(t)$ (highlighted in red in Table 3) rather than the yearly averaged $M_r^I(t)$ (highlighted in blue). This narrows the selection down to models C2, E2, and F2. Models C2 and F2 are equivalent, only for their main spatial covariate, with C2 using $\sigma_c(\mathbf{s})$ and F2 using $C(\mathbf{s})$. Model F2 outperforms model C2 in n-fold CV, while model C2 outperforms model F2 in spatio-temporal CV by the same very small margin. In both models F2 and C2, the coefficient β_3 of the spatio-temporal interaction between $C(\mathbf{s})$ and $M^I(t)$ was not statistically significant with 95% confidence bounds containing 0. In this regard, we prefer model E2 over F2, since E2 is a nested model of F2, simply without the spatio-temporal interaction. We note that model F2 gives a very slight improvement in n-fold CRPS CV yet no improvement in spatio-temporal CV. Comparing models C2 and E2, both with very similar CV metrics and considering the earlier discussion of base model H3 outperforming H2, we prefer model E2. Finally, we choose model E2 for its parsimony, predictive and modelling performance, and ease of interpretation.

To summarise, our chosen marginal GPD model E2 uses coastal proximity, $C(\mathbf{s})$, as a spatial covariate, smoothed temperature anomalies over Ireland, $M^I(t)$, as a long-term temporal covariate, and monthly residuals from smoothed covariate, $M_{r,m}^I(t)$, as a SVC covariate, capturing unusually cold winters. To assess the absolute quality of the chosen model E2, we create a pooled QQ-plot in the right-hand panel of Figure 13, pooling over all sites and years. We transform the data through our fitted model into a common uniform scale and to a common exponential scale. The exponential scale accentuates the upper tail of the data and highlights the model’s performance in capturing the extreme values. We see evidence of a good fit, with values near the lines of equality, and in the far upper tail, all values falling within the pointwise tolerance bounds. The left-hand plot of the same figure presents the equivalent plot, but using model E1 (equivalent to model E2 but with no covariate $z(t)$ to capture SCV). This clearly highlights how not accounting for climate variability in extreme

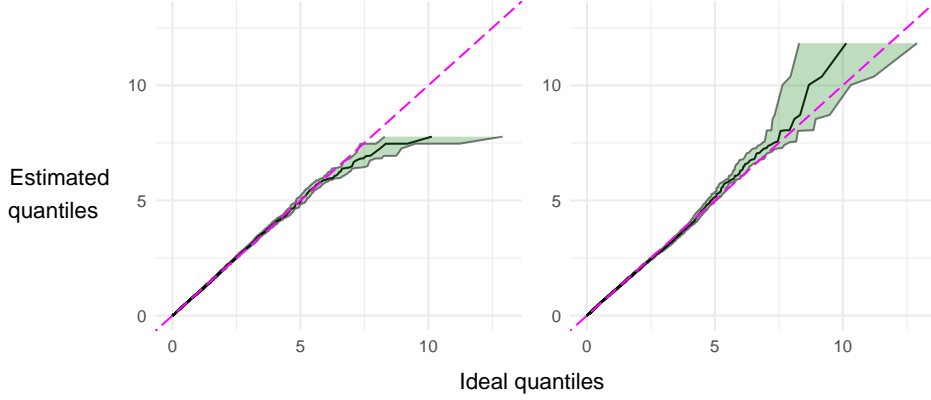


Figure 13: QQ-plot of two models on exponential margins to accentuate the behaviour of the tail. Model E1 without climate oscillation covariate (left), final chosen model E2 with climate oscillation covariate (right)

winter temperatures leads to a poor representation of the data in the upper tail. This leads to model E1 having a heavier tail ($\hat{\xi} = 0.011$) than our preferred model E2 ($\hat{\xi} = -0.079$) and thus, overestimates the heaviness of the tail of the distribution.

Figure 14 plots the scale parameter, σ , estimated via model E2. This figure shows that the most variable excess distribution is inland, with a decay in values moving towards the coast, highlighting the ocean’s regulatory effect. Furthermore, we see the largest estimated scale parameter at higher levels of SCV. The estimated change in the scale parameter over the observation period denoted $\nabla\sigma_o(\mathbf{s})$, during low, median, and high phases of SCV, is plotted on the bottom row of the same figure. The scale parameter has decreased overall levels of SCV with the largest decrease during phases of high SCV. Recall that we are modelling the maximum of negative minimum temperatures (see Equation (1)), so the decreasing scale parameter suggests a warming of extreme minimum winter temperatures, with the greatest warming observed during high levels of SCV.

Table 3: Cross-validation metrics for each GPD model.

Model	Parameterisation of $\ln \sigma_o$	ST-CV		n-CV	
		RMSE	CRPS	RMSE	CRPS
A 1	$\beta_0 + \beta_1 M^I(t)$	1.223	0.886	1.350	0.946
2	$\beta_0 + \beta_1 M^I(t) + \beta_2 M_{r,m}^I(t)$	-	0.824	-	0.880
3	$\beta_0 + \beta_1 M^I(t) + \beta_2 M_r^I(t)$	1.106	0.836	1.198	0.895
4	$\beta_0 + \beta_1 M^I(t) + \beta_2 M_r^G(t)$	1.122	0.842	1.221	0.901
5	$\beta_0 + \beta_1 M^I(t) + \beta_2 M_r^G(t)$	1.128	0.848	1.224	0.906
6	$\beta_0 + \beta_1 M^I(t) + \beta_2 AO(t)$	1.112	0.842	1.208	0.901
7	$\beta_0 + \beta_1 M^I(t) + \beta_2 AO_r(t)$	1.112	0.842	1.208	0.901
8	$\beta_0 + \beta_1 M^I(t) + \beta_2 AO_m(t)$	-	0.862	-	0.918
9	$\beta_0 + \beta_1 M^I(t) + \beta_2 AO_{r,m}(t)$	-	0.862	-	0.918
10	$\beta_0 + \beta_1 M^I(t) + \beta_2 NAO(t)$	1.121	0.843	1.220	0.904
11	$\beta_0 + \beta_1 M^I(t) + \beta_2 NAO_r(t)$	1.121	0.843	1.220	0.904
12	$\beta_0 + \beta_1 M^I(t) + \beta_2 NAO_m(t)$	-	0.845	-	0.902
13	$\beta_0 + \beta_1 M^I(t) + \beta_2 NAO_{r,m}(t)$	-	0.845	-	0.902
B 1	$\beta_0 + \beta_1 \sigma_c(\mathbf{s}) + \beta_2 M^I(t)$	1.225	0.887	1.349	0.946
2	$\beta_0 + \beta_1 \sigma_c(\mathbf{s}) + \beta_2 M^I(t) + \beta_3 M_{r,m}^I(t)$	-	0.823	-	0.880
3	$\beta_0 + \beta_1 \sigma_c(\mathbf{s}) + \beta_2 M^I(t) + \beta_3 M_r^I(t)$	1.110	0.836	1.199	0.895
4	$\beta_0 + \beta_1 \sigma_c(\mathbf{s}) + \beta_2 M^I(t) + \beta_3 M_r^G(t)$	1.126	0.843	1.222	0.901
5	$\beta_0 + \beta_1 \sigma_c(\mathbf{s}) + \beta_2 M^I(t) + \beta_3 M_r^G(t)$	1.130	0.848	1.224	0.906
6	$\beta_0 + \beta_1 \sigma_c(\mathbf{s}) + \beta_2 M^I(t) + \beta_3 AO(t)$	1.116	0.842	1.208	0.901
7	$\beta_0 + \beta_1 \sigma_c(\mathbf{s}) + \beta_2 M^I(t) + \beta_3 AO_r(t)$	1.115	0.842	1.208	0.901

8	$\beta_0 + \beta_1\sigma_c(\mathbf{s}) + \beta_2M^I(t) + \beta_3AO_m(t)$	-	0.862	-	0.918
9	$\beta_0 + \beta_1\sigma_c(\mathbf{s}) + \beta_2M^I(t) + \beta_3AO_{r,m}(t)$	-	0.862	-	0.918
10	$\beta_0 + \beta_1\sigma_c(\mathbf{s}) + \beta_2M^I(t) + \beta_3NAO(t)$	1.125	0.844	1.220	0.903
11	$\beta_0 + \beta_1\sigma_c(\mathbf{s}) + \beta_2M^I(t) + \beta_3NAO_r(t)$	1.125	0.843	1.220	0.903
12	$\beta_0 + \beta_1\sigma_c(\mathbf{s}) + \beta_2M^I(t) + \beta_3NAO_m(t)$	-	0.845	-	0.902
13	$\beta_0 + \beta_1\sigma_c(\mathbf{s}) + \beta_2M^I(t) + \beta_3NAO_{r,m}(t)$	-	0.845	-	0.902
C 1	$\beta_0 + \beta_1\sigma_c(\mathbf{s}) + \beta_2M^I(t) + \beta_3M^I(t)C(\mathbf{s})$	1.189	0.879	1.320	0.939
2	$\beta_0 + \beta_1\sigma_c(\mathbf{s}) + \beta_2M^I(t) + \beta_3M^I(t)C(\mathbf{s}) + \beta_4M_{r,m}^I(t)$	-	0.815	-	0.874
3	$\beta_0 + \beta_1\sigma_c(\mathbf{s}) + \beta_2M^I(t) + \beta_3M^I(t)C(\mathbf{s}) + \beta_4M_r^I(t)$	1.064	0.828	1.166	0.889
4	$\beta_0 + \beta_1\sigma_c(\mathbf{s}) + \beta_2M^I(t) + \beta_3M^I(t)C(\mathbf{s}) + \beta_4M_r^G(t)$	1.083	0.835	1.188	0.895
5	$\beta_0 + \beta_1\sigma_c(\mathbf{s}) + \beta_2M^I(t) + \beta_3M^I(t)C(\mathbf{s}) + \beta_4M_r^G(t)$	1.087	0.840	1.191	0.899
6	$\beta_0 + \beta_1\sigma_c(\mathbf{s}) + \beta_2M^I(t) + \beta_3M^I(t)C(\mathbf{s}) + \beta_4AO(t)$	1.075	0.834	1.176	0.895
7	$\beta_0 + \beta_1\sigma_c(\mathbf{s}) + \beta_2M^I(t) + \beta_3M^I(t)C(\mathbf{s}) + \beta_4AO_r(t)$	1.073	0.834	1.177	0.896
8	$\beta_0 + \beta_1\sigma_c(\mathbf{s}) + \beta_2M^I(t) + \beta_3M^I(t)C(\mathbf{s}) + \beta_4AO_m(t)$	-	0.855	-	0.911
9	$\beta_0 + \beta_1\sigma_c(\mathbf{s}) + \beta_2M^I(t) + \beta_3M^I(t)C(\mathbf{s}) + \beta_4AO_{r,m}(t)$	-	0.855	-	0.911
10	$\beta_0 + \beta_1\sigma_c(\mathbf{s}) + \beta_2M^I(t) + \beta_3M^I(t)C(\mathbf{s}) + \beta_4NAO(t)$	1.085	0.838	1.186	0.898
11	$\beta_0 + \beta_1\sigma_c(\mathbf{s}) + \beta_2M^I(t) + \beta_3M^I(t)C(\mathbf{s}) + \beta_4NAO_r(t)$	1.077	0.835	1.187	0.898
12	$\beta_0 + \beta_1\sigma_c(\mathbf{s}) + \beta_2M^I(t) + \beta_3M^I(t)C(\mathbf{s}) + \beta_4NAO_m(t)$	-	0.838	-	0.896
13	$\beta_0 + \beta_1\sigma_c(\mathbf{s}) + \beta_2M^I(t) + \beta_3M^I(t)C(\mathbf{s}) + \beta_4NAO_{r,m}(t)$	-	0.838	-	0.896
D 1	$\beta_0 + \beta_1\sigma_c(\mathbf{s}) + \beta_2M^I(t) + \beta_3M^I(t)C(\mathbf{s})$	1.225	0.887	1.349	0.945
2	$\beta_0 + \beta_1\sigma_c(\mathbf{s}) + \beta_2M^I(t) + \beta_3M^I(t)C(\mathbf{s}) + \beta_4M_{r,m}^I(t)$	-	0.824	-	0.880
3	$\beta_0 + \beta_1\sigma_c(\mathbf{s}) + \beta_2M^I(t) + \beta_3M^I(t)C(\mathbf{s}) + \beta_4M_r^I(t)$	1.112	0.837	1.200	0.895
4	$\beta_0 + \beta_1\sigma_c(\mathbf{s}) + \beta_2M^I(t) + \beta_3M^I(t)C(\mathbf{s}) + \beta_4M_r^G(t)$	1.125	0.844	1.222	0.902
5	$\beta_0 + \beta_1\sigma_c(\mathbf{s}) + \beta_2M^I(t) + \beta_3M^I(t)C(\mathbf{s}) + \beta_4M_r^G(t)$	1.131	0.849	1.224	0.906
6	$\beta_0 + \beta_1\sigma_c(\mathbf{s}) + \beta_2M^I(t) + \beta_3M^I(t)C(\mathbf{s}) + \beta_4AO(t)$	1.117	0.842	1.208	0.901
7	$\beta_0 + \beta_1\sigma_c(\mathbf{s}) + \beta_2M^I(t) + \beta_3M^I(t)C(\mathbf{s}) + \beta_4AO_r(t)$	1.116	0.842	1.208	0.901
8	$\beta_0 + \beta_1\sigma_c(\mathbf{s}) + \beta_2M^I(t) + \beta_3M^I(t)C(\mathbf{s}) + \beta_4AO_m(t)$	-	0.863	-	0.918
9	$\beta_0 + \beta_1\sigma_c(\mathbf{s}) + \beta_2M^I(t) + \beta_3M^I(t)C(\mathbf{s}) + \beta_4AO_{r,m}(t)$	-	0.863	-	0.918
10	$\beta_0 + \beta_1\sigma_c(\mathbf{s}) + \beta_2M^I(t) + \beta_3M^I(t)C(\mathbf{s}) + \beta_4NAO(t)$	1.123	0.843	1.219	0.904
11	$\beta_0 + \beta_1\sigma_c(\mathbf{s}) + \beta_2M^I(t) + \beta_3M^I(t)C(\mathbf{s}) + \beta_4NAO_r(t)$	1.122	0.844	1.222	0.904
12	$\beta_0 + \beta_1\sigma_c(\mathbf{s}) + \beta_2M^I(t) + \beta_3M^I(t)C(\mathbf{s}) + \beta_4NAO_m(t)$	-	0.845	-	0.902
13	$\beta_0 + \beta_1\sigma_c(\mathbf{s}) + \beta_2M^I(t) + \beta_3M^I(t)C(\mathbf{s}) + \beta_4NAO_{r,m}(t)$	-	0.844	-	0.902
E 1	$\beta_0 + \beta_1C(\mathbf{s}) + \beta_2M^I(t)$	1.189	0.878	1.320	0.939
2	$\beta_0 + \beta_1C(\mathbf{s}) + \beta_2M^I(t) + \beta_3M_{r,m}^I(t)$	-	0.816	-	0.874
3	$\beta_0 + \beta_1C(\mathbf{s}) + \beta_2M^I(t) + \beta_3M_r^I(t)$	1.065	0.829	1.163	0.888
4	$\beta_0 + \beta_1C(\mathbf{s}) + \beta_2M^I(t) + \beta_3M_r^G(t)$	1.080	0.834	1.187	0.895
5	$\beta_0 + \beta_1C(\mathbf{s}) + \beta_2M^I(t) + \beta_3M_r^G(t)$	1.086	0.840	1.190	0.899
6	$\beta_0 + \beta_1C(\mathbf{s}) + \beta_2M^I(t) + \beta_3AO(t)$	1.073	0.834	1.176	0.895
7	$\beta_0 + \beta_1C(\mathbf{s}) + \beta_2M^I(t) + \beta_3AO_r(t)$	1.073	0.834	1.176	0.895
8	$\beta_0 + \beta_1C(\mathbf{s}) + \beta_2M^I(t) + \beta_3AO_m(t)$	-	0.855	-	0.912
9	$\beta_0 + \beta_1C(\mathbf{s}) + \beta_2M^I(t) + \beta_3AO_{r,m}(t)$	-	0.855	-	0.911
10	$\beta_0 + \beta_1C(\mathbf{s}) + \beta_2M^I(t) + \beta_3NAO(t)$	1.081	0.836	1.187	0.898
11	$\beta_0 + \beta_1C(\mathbf{s}) + \beta_2M^I(t) + \beta_3NAO_r(t)$	1.081	0.836	1.187	0.898
12	$\beta_0 + \beta_1C(\mathbf{s}) + \beta_2M^I(t) + \beta_3NAO_m(t)$	-	0.837	-	0.896
13	$\beta_0 + \beta_1C(\mathbf{s}) + \beta_2M^I(t) + \beta_3NAO_{r,m}(t)$	-	0.837	-	0.896
F 1	$\beta_0 + \beta_1C(\mathbf{s}) + \beta_2M^I(t) + \beta_3M^I(t)C(\mathbf{s})$	1.187	0.878	1.316	0.938
2	$\beta_0 + \beta_1C(\mathbf{s}) + \beta_2M^I(t) + \beta_3M^I(t)C(\mathbf{s}) + \beta_4M_{r,m}^I(t)$	-	0.816	-	0.873
3	$\beta_0 + \beta_1C(\mathbf{s}) + \beta_2M^I(t) + \beta_3M^I(t)C(\mathbf{s}) + \beta_4M_r^I(t)$	1.063	0.828	1.159	0.888
4	$\beta_0 + \beta_1C(\mathbf{s}) + \beta_2M^I(t) + \beta_3M^I(t)C(\mathbf{s}) + \beta_4M_r^G(t)$	1.079	0.835	1.181	0.894
5	$\beta_0 + \beta_1C(\mathbf{s}) + \beta_2M^I(t) + \beta_3M^I(t)C(\mathbf{s}) + \beta_4M_r^G(t)$	1.083	0.840	1.183	0.898
6	$\beta_0 + \beta_1C(\mathbf{s}) + \beta_2M^I(t) + \beta_3M^I(t)C(\mathbf{s}) + \beta_4AO(t)$	1.072	0.835	1.172	0.895
7	$\beta_0 + \beta_1C(\mathbf{s}) + \beta_2M^I(t) + \beta_3M^I(t)C(\mathbf{s}) + \beta_4AO_r(t)$	1.069	0.833	1.171	0.895
8	$\beta_0 + \beta_1C(\mathbf{s}) + \beta_2M^I(t) + \beta_3M^I(t)C(\mathbf{s}) + \beta_4AO_m(t)$	-	0.854	-	0.911
9	$\beta_0 + \beta_1C(\mathbf{s}) + \beta_2M^I(t) + \beta_3M^I(t)C(\mathbf{s}) + \beta_4AO_{r,m}(t)$	-	0.854	-	0.911
10	$\beta_0 + \beta_1C(\mathbf{s}) + \beta_2M^I(t) + \beta_3M^I(t)C(\mathbf{s}) + \beta_4NAO(t)$	1.081	0.836	1.185	0.897
11	$\beta_0 + \beta_1C(\mathbf{s}) + \beta_2M^I(t) + \beta_3M^I(t)C(\mathbf{s}) + \beta_4NAO_r(t)$	1.082	0.836	1.184	0.897
12	$\beta_0 + \beta_1C(\mathbf{s}) + \beta_2M^I(t) + \beta_3M^I(t)C(\mathbf{s}) + \beta_4NAO_m(t)$	-	0.837	-	0.895
13	$\beta_0 + \beta_1C(\mathbf{s}) + \beta_2M^I(t) + \beta_3M^I(t)C(\mathbf{s}) + \beta_4NAO_{r,m}(t)$	-	0.837	-	0.895
G 1	$\beta_0 + \beta_1M^I(t) + \beta_2M^I(t)C(\mathbf{s})$	1.224	0.886	1.349	0.945

2	$\beta_0 + \beta_1 M^I(t) + \beta_2 M^I(t)C(\mathbf{s}) + \beta_4 M_{r,m}^I(t)$	-	0.824	-	0.880
3	$\beta_0 + \beta_1 M^I(t) + \beta_2 M^I(t)C(\mathbf{s}) + \beta_4 M_r^I(t)$	1.107	0.836	1.198	0.895
4	$\beta_0 + \beta_1 M^I(t) + \beta_2 M^I(t)C(\mathbf{s}) + \beta_4 M_r^G(t)$	1.122	0.843	1.221	0.901
5	$\beta_0 + \beta_1 M^I(t) + \beta_2 M^I(t)C(\mathbf{s}) + \beta_4 M_r^G(t)$	1.129	0.849	1.224	0.906
6	$\beta_0 + \beta_1 M^I(t) + \beta_2 M^I(t)C(\mathbf{s}) + \beta_4 \text{AO}(t)$	1.113	0.842	1.208	0.901
7	$\beta_0 + \beta_1 M^I(t) + \beta_2 M^I(t)C(\mathbf{s}) + \beta_4 \text{AO}_r(t)$	1.113	0.842	1.208	0.901
8	$\beta_0 + \beta_1 M^I(t) + \beta_2 M^I(t)C(\mathbf{s}) + \beta_4 \text{AO}_m(t)$	-	0.862	-	0.918
9	$\beta_0 + \beta_1 M^I(t) + \beta_2 M^I(t)C(\mathbf{s}) + \beta_4 \text{AO}_{r,m}(t)$	-	0.862	-	0.918
10	$\beta_0 + \beta_1 M^I(t) + \beta_2 M^I(t)C(\mathbf{s}) + \beta_4 \text{NAO}(t)$	1.124	0.844	1.220	0.904
11	$\beta_0 + \beta_1 M^I(t) + \beta_2 M^I(t)C(\mathbf{s}) + \beta_4 \text{NAO}_r(t)$	1.122	0.844	1.221	0.904
12	$\beta_0 + \beta_1 M^I(t) + \beta_2 M^I(t)C(\mathbf{s}) + \beta_4 \text{NAO}_m(t)$	-	0.845	-	0.902
13	$\beta_0 + \beta_1 M^I(t) + \beta_2 M^I(t)C(\mathbf{s}) + \beta_4 \text{NAO}_{r,m}(t)$	-	0.845	-	0.902
H 1	β_0	1.224	0.885	1.354	0.945
2	$\beta_0 + \beta_1 \sigma_c(\mathbf{s})$	1.225	0.885	1.354	0.945
3	$\beta_0 + \beta_1 C(\mathbf{s})$	1.189	0.878	1.322	0.939

3.3.6 Bootstrapping procedure

We rely on bootstrapping to characterise and propagate the uncertainty in our modelling assumptions throughout the entire analysis, from the marginal bulk and tail model to the r -Pareto simulations. We use a bootstrapping algorithm designed to preserve spatial and short-term temporal dependence in the process, while also matching missingness patterns in the observation data. This can be achieved through vector temporal block bootstrapping of the observed data after being transformed to be uniformly distributed, $X_o^U(t, \mathbf{s}) = F_{t,\mathbf{s}}^{-1}\{X_o(t, \mathbf{s})\}$, where $F_{t,\mathbf{s}}$ represents the distribution function of the process at time t and site \mathbf{s} , constructed as a combination of the bulk and tail models derived earlier. The resampled data are then transformed back to the data scale, giving a bootstrapped sample data set, $X_o^*(t, \mathbf{s})$, generated under the chosen marginal model.

We adapt the bootstrapping procedure proposed by Healy et al. (2024), which was not immediately applicable to our winter data set for two reasons. Firstly, the authors focused on summer temperatures, however, our dataset of extremely cold winter events presented substantially stronger temporal dependence which the bootstrapping algorithm needed to account for. Secondly, we found that temporal trends in cold winter extremes were much more variable and more complex in terms of dependence on climate indicators than in hot summer extremes. Here we describe modifications to the bootstrapping algorithm to account for these features and capture them in the bootstrap samples.

Solar insolation is lowest in Ireland during winter months and so factors such as clouds tend to have much lower local impact leading to more spatially and temporally smooth structures (Liou, 2002). Through exploratory analysis, we found the expected duration of an extreme cold event at any site was approximately 20 days on average, see Figure 15. Temporally de-clustering extreme events at a single site would create independent observations and remove the need to perform block bootstrapping. However, in a spatio-temporal setting, de-clustering each site separately would greatly increase the permutations of observed sites across each day, greatly reducing the number of possible spatial matches for resampling.

Instead, we summarise all days in the data set by the minimum temperature observed across sites on that day, creating a time series of $\min_{\mathbf{s} \in \mathcal{S}} \{X(t, \mathbf{s})\}$, as shown in Figure 16. We considered two approaches using this series. By temporally de-clustering this time series, taking local minima within a ± 10 day range, and keeping all data within the de-clustered dates gives approximately independent observations without disrupting the spatial dimension. However, this risks under-representing areas that experience less severe extremes while also being wasteful of data. Instead, we create spatio-temporal blocks on the original data, centred on the de-clustered local minima of $\min_{\mathbf{s} \in \mathcal{S}} \{X(t, \mathbf{s})\}$, extending to the midpoint between the previous and subsequent local minima. These blocks are assumed to be independent and capture the short-range temporal dependence in the data. We found the best results when we extended the range for declustering to a ± 15 day range, allowing us to capture

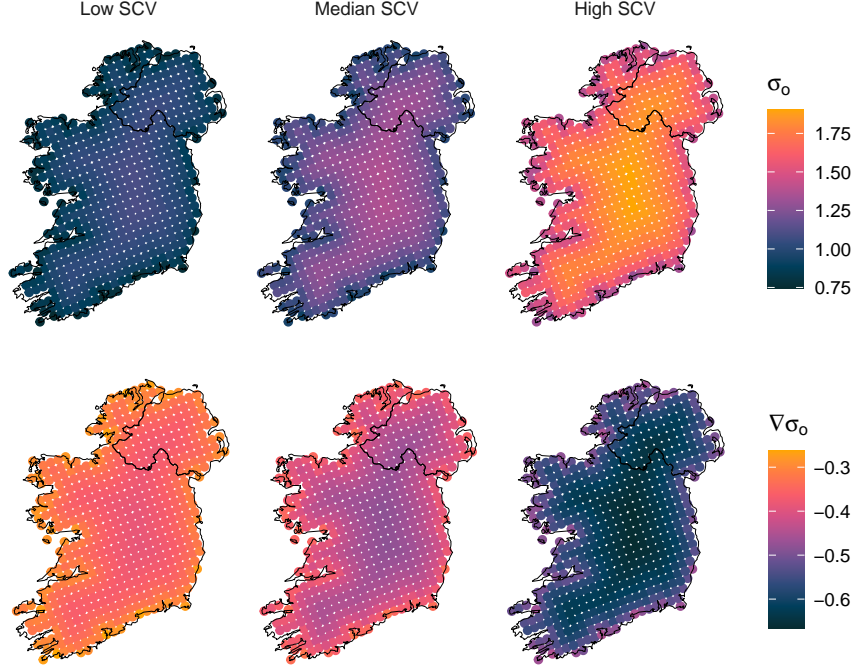


Figure 14: Estimated GPD scale parameter according to model E2 in 2022 during low, median, and high phases of SCV (top row, left to right respectively). Estimated change in the scale parameter since 1950, $\nabla\sigma_o(\mathbf{s})$ with respect to scale estimates during low, median, and high phases of SCV as plotted above (bottom row, left to right respectively).

the majority of the events with very strong autocorrelation while being small enough to allow us to define a suitably large number of blocks for resampling. The de-clustered local minima are highlighted in red in Figure 16.

A key issue with the bootstrapping procedure presented by Healy et al. (2024) is that it assumes the model is correct and that $F_{t,\mathbf{s}}\{X_o(t,\mathbf{s})\}$ is uniformly distributed. Assuming that the model captures all temporal non-stationarity within the data is certainly unrealistic when the non-stationarity is complex, and highly variable, and the choice of the best-performing model is not obvious. Our aim is to capture and accurately describe the overarching trend of winter extremes in Ireland, disentangling the long-term trend from complex climatic variations. Furthermore, we found that the most extreme events (such as winter 2009/10, as discussed in Section 1) greatly affected extremal inference on that bootstrapped data set. As is shown in Figure 2, the winter of 2009/2010 constitutes a disproportionately large portion of extremal observations and hence is more likely to be resampled. With the aim of preserving the global trend of the data, in the context of numerous and highly variable models, while accurately representing expected large variation, we restrict resampling within windows of ± 10 years. We accept a resample if it is within a 10-year window of the data being replaced.

When resampling, we initially only accepted resampled blocks if they had the exact spatio-temporal pattern as the block being replaced as a subset of its data. Given our set of fixed and predefined blocks, this led to relatively few suitable choices available to resample, leading to little variation in the bootstrapped data sets. To deal with this, we experimented with a “relaxed” resampling algorithm for spatial pattern matching. We accepted a resampled block if it had a high proportion of the sites in the block it was replacing. We found that we had sufficient variation when accepting blocks that had 90% of the sites being replaced. To preserve missingness patterns in the data we discarded observations from sites in the resampled block that are not in the block that was being replaced. If the resampled block was of a longer duration than the block being replaced we took a subset of the

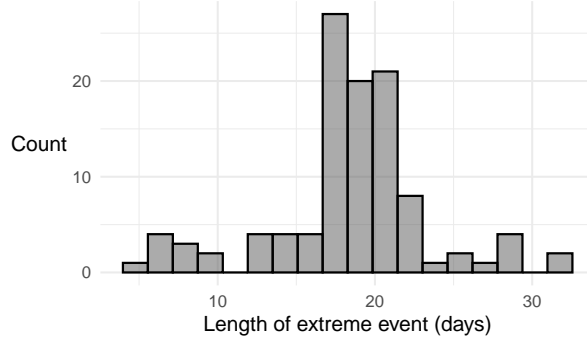


Figure 15: The mean across all sites of the length of extreme events in days. The duration of a single extreme event is the number of consecutive extreme observations that occur within a seven-day period of another at an individual site.

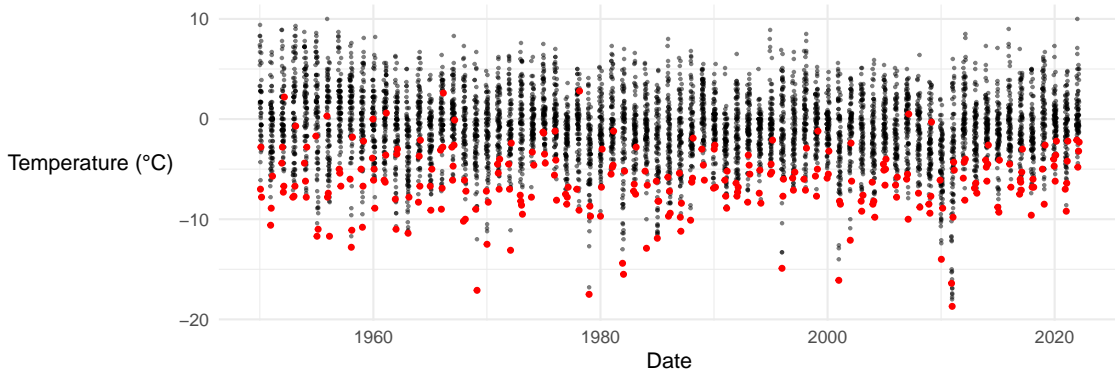


Figure 16: Time series of $\min_{\mathbf{s} \in \mathcal{S}} \{X(t, \mathbf{s})\}$ over the period 1950–2022 with de-clustered local minima (in ± 15 days) highlighted in red.

resampled block, randomly.

4 Multivariate dependence models

4.1 Overview and strategy

We investigate the level of extremal dependence of extreme minimum daily winter temperature data. We first standardise the marginal variables so that they have an identical distribution over variables and covariates such that we can fairly investigate extremal dependence. We transform the data to uniform margins using the probability integral transform, and following this, we transform to standard Pareto using

$$X^P(t, \mathbf{s}) = \frac{1}{1 - F_{t, \mathbf{s}}\{X(t, \mathbf{s})\}}, \text{ for all } \mathbf{s} \in \mathcal{S} \text{ and all } t, \quad (5)$$

where $F_{t, \mathbf{s}}$ is the estimated distribution function of $X(t, \mathbf{s})$ with quantile regression bulk model below $u(\mathbf{s})$ and GPD tail model above. Following this, we fit a generalised r -Pareto process to extreme spatial observations as decided via a cost function to model the extremal dependence. Asymptotic dependence is a prerequisite for fitting the r -Pareto model and so we test if the data satisfies this requirement. A discussion of the extremal dependence of the data is shown in Section 4.2. After fitting the r -Pareto process (covered in Section 4.3) we generate spatial simulations under different phases of SCV.

4.2 Evidence for asymptotic dependence

The pairwise coefficient of asymptotic dependence, χ , measures the probability of a process at two sites being jointly extreme (Coles et al., 1999). Recall, for the process X^P at sites \mathbf{s}_i and \mathbf{s}_j , $\chi = \chi^P(\mathbf{s}_i, \mathbf{s}_j)$ is defined by

$$\chi^P(\mathbf{s}_i, \mathbf{s}_j) = \lim_{v \rightarrow \infty} \Pr(X^P(\mathbf{s}_j) > v | X^P(\mathbf{s}_i) > v) \quad (6)$$

If $\chi^P(\mathbf{s}_i, \mathbf{s}_j) > 0$ (or equals 0) then process X^P is asymptotically dependent (or asymptotically independent) at this pair of sites respectively. The value of χ ($0 < \chi \leq 1$) determines the degree of asymptotic dependence, with χ increasing as this dependence strengthens.

We define an empirical estimator of the tail coefficient of processes X_1 and X_2 at quantile u as

$$\chi_u(X_1, X_2) = \frac{P[F_{X_1}(X_1) > u, F_{X_2}(X_2) > u]}{P[F_{X_2}(X_2) > u]}, \quad (7)$$

where F_{X_i} denotes the distribution function of process X_i . Empirical estimates of χ are plotted against the distance between sites for all pairs of sites for both the observational data, X_o^P , and climate model data X_c^P in Figure 17. This figure suggests that the climate model output overestimates extremal dependence in observational winter temperatures. The empirically estimated coefficient of extremal dependence for both processes remains non-zero, even at considerable distances and increasing quantiles with the magnitude of χ changes minimally as quantiles increase. Our analysis suggests that the assumption of asymptotic dependence in the minimum daily temperature in Ireland is reasonable.

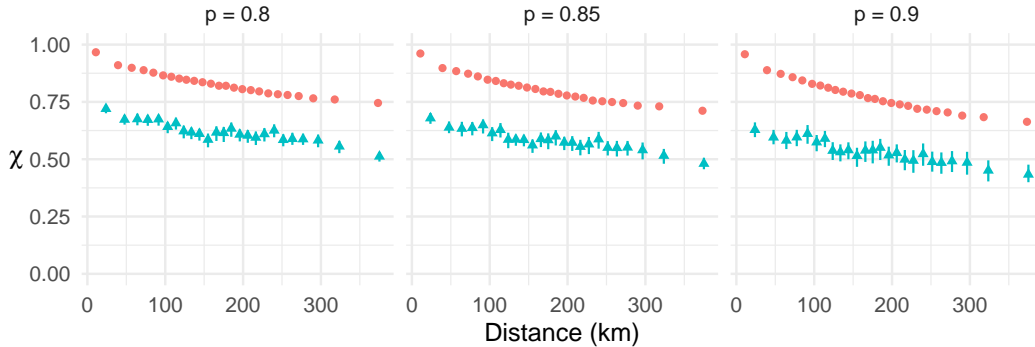


Figure 17: Estimates of χ plotted against inter-site distance for observational data (blue), standardised using marginal model E2, and climate model output (orange) for $u = 0.8, 0.85,$ and 0.9 with 95% confidence intervals plotted as vertical lines.

4.3 r -Pareto process

After standardising the data to unit Pareto margins, we model the extreme dependence of the process $X^P(t, \mathbf{s})$ over $\mathbf{s} \in \mathcal{S}$ with an r -Pareto process (Dombry and Ribatet, 2015; de Fondeville and Davison, 2018). We define a risk function to provide a measure and ordering to levels of extremity of spatial observations, $r(X^P) := r\{X^P(\mathbf{s}) : \mathbf{s} \in \mathcal{S}\} \in [0, \infty)$, where r must be homogeneous of order 1. Under weak conditions on the process X^P , we have that

$$\Pr\{v^{-1}X^P(\mathbf{s} : \mathbf{s} \in \mathcal{S}) \in \cdot \mid r(X^P(\mathbf{s} : \mathbf{s} \in \mathcal{S})) > v\} \rightarrow \Pr\{Y_r^P(\mathbf{s} : \mathbf{s} \in \mathcal{S}) \in \cdot\}, \quad (8)$$

as $v \rightarrow \infty$, where $\{Y_r^P(\mathbf{s}) : \mathbf{s} \in \mathcal{S}\}$ is marginally non-degenerate in any margins. Here, Y_r^P is called the r -Pareto process. If the limit provided in Equation (8) is a good approximation for large v , then

those spatial events with a risk function exceeding v will be well-approximated by an r -Pareto process. Crucially, Y_r^P can be decomposed into two independent stochastic components as follows:

$$Y_r^P(\mathbf{s}) = RW(\mathbf{s}) \text{ for all } \mathbf{s} \in \mathcal{S} \quad (9)$$

where R is Pareto distributed and can be interpreted as the risk of the process, and $\{W(\mathbf{s}) : \mathbf{s} \in \mathcal{S}\}$ is a stochastic process which describes the spatial profile of the extreme event, i.e., the proportion of the risk at each site. By construction, we have that $R = r(Y_r^P(\mathbf{s} : \mathbf{s} \in \mathcal{S}))$ and $r(W(\mathbf{s} : \mathbf{s} \in \mathcal{S})) = 1$, where $R \sim \text{Pareto}(1)$ can be interpreted as the magnitude or cost of the process, i.e., $R = r(Y)$. The spatial process of Y is then W . This characterisation is powerful as it allows extrapolation to events larger than those previously observed.

We take the cost function to be

$$r_t(X_o^P(t, \mathbf{s}) : \mathbf{s} \in \mathcal{S}) = \frac{\sum_{i=1}^d X_o^P(t, \mathbf{s}_i) I_o(t, \mathbf{s}_i)}{\sum_{i=1}^d I_o(t, \mathbf{s}_i)},$$

where $I_o(t, \mathbf{s}_i)$ is the indicator variable for whether $X_o(t, \mathbf{s}_i)$ is observed or not, d is the number of sampling locations selected for the risk function evaluation using sites $\mathbf{s}_1, \dots, \mathbf{s}_d$. Thus, the risk function r_t is the average of standardised variables over the d sites which were observed at time t , and so is invariant to the changing dimension of the partially observed event.

Expression (9) allows us to model the spatial profile of extremal dependence separately from the magnitude. Furthermore, the choice of a parametric spatial process W also affords great flexibility. Following de Fondeville and Davison (2018) and Palacios-Rodríguez et al. (2020), we choose to model W using the log-Gaussian stochastic process (also referred to as the Brown–Resnick process in the max-stable literature). Modelling the angular component W of the r -Pareto process via log-Gaussian processes affords us the ability to make use of classical geostatistical methods. Engelke et al. (2015) note that the finite-dimensional marginal distribution of the log-Gaussian process at sites s_0, s_1, \dots, s_k is the Hüsler-Reiss distribution (Hüsler and Reiss, 1989) with spectral density h and parameter matrix $\Lambda = (\lambda_{i,j}^2)_{0 \leq i, j \leq k} = (\gamma(s_i - s_j)/2)_{0 \leq i, j \leq k}$. So, we can express h in terms of this variogram γ . We use the Matérn variogram family

$$\gamma_{\text{mat}}(h; t) = \alpha \{1 - (2\sqrt{\nu}h/\phi)^\nu 2^{1-\nu} \Gamma(\nu)^{-1} K_\nu(2\sqrt{\nu}h/\phi)\}, \quad (10)$$

for inter-site distance $h \geq 0$, K_ν a modified Bessel function of the second kind, and the positive parameters (α, ϕ, ν) which determine the variance, range, and smoothness, respectively (Banerjee et al., 2014).

In general, the estimation of the smoothness parameter, ν , is difficult in practice (Bai et al., 2012). A popular approach to alleviate this issue is to estimate ν via a grid search (Ip and K., 2017). We fit the r -Pareto process over a grid of values for ν and found that $\nu = 0.1$ maximised the likelihood function. We found the risk threshold we used to model extreme extremal dependence for summer temperature data provided an accurate choice for modelling winter minima. That is, we choose events whose risk is above the 80% quantile of the risks calculated for all observed events. Figure 18 shows the estimated χ_o^P derived from the fitted r -Pareto process with associated 95% uncertainty bounds based on 200 spatio-temporal bootstrap samples, along with the pairwise empirical estimator as in expression (7), estimated for a high quantile ($u = 0.92$). The figure shows a good fit to the data, suggesting the r -Pareto process is capturing the level of asymptotic dependence well. We tested for linear non-stationarity in the scale and range parameters of the Matérn variogram, α and ϕ respectively. We use year, scaled between 0 and 1, as a temporal covariate. However, we do not find any statistically significant evidence for change in the variogram's parameters.

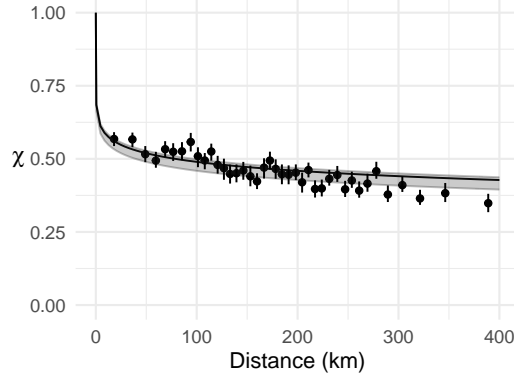


Figure 18: Estimates of χ_o^P against inter-site distance h for model E2: the pairwise empirical estimator of χ_o^P for $u = 0.92$, calculated as in expression (7) is shown as vertical line segments reflecting the bootstrap uncertainty in the marginal distribution estimates; the smooth lines display the limiting value for χ_o^P , estimated using the r -Pareto process with a Matérn variogram when fitted above an 80% risk threshold, with 95% confidence intervals, capturing both marginal and extremal dependence bootstrap uncertainties.

5 Results

In this section, we present a range of summaries of how daily minimum winter temperature extreme events in Ireland are changing over the period 1950–2022. Firstly, we characterise how winter temperature extremes are changing on a marginal level in Section 5.1. Following this, in Section 5.2, we summarise temporal non-stationarities in the spatial context. We present a range of extremal simulation summary statistics detailing how spatial daily minimum temperature extreme events in Ireland are changing over the period 1950–2022. Throughout this section, we present results in the context of low, median, and high SCV.

5.1 Marginal return level results

Figure 19 presents estimates of the 100-year return level in the context of the year 2022 for model E2. The 100-year level corresponds to an occurrence probability of $1/(100 \times 90.25)$. In this figure, we see the return level associated with different phases of SCV, i.e., $M_{r,m}^{(0.1,I)}(t)$, $M_{r,m}^{(0.5,I)}(t)$, and $M_{r,m}^{(0.9,I)}(t)$, from left to right. The figure clearly shows that, in lower phases of SCV, we see much less extreme temperatures. We estimate a return level of -8.9°C to -2.7°C over Ireland associated with the covariate level $M_{r,m}^{(0.1,I)}(t)$ corresponding to the low phase of SCV. At increasing levels of SCV, we see more intense return levels, i.e., we estimate a return level of -10.9°C to -3.9°C and -14.6°C to -6.8°C associated to the levels $M_{r,m}^{(0.5,I)}(t)$ and $M_{r,m}^{(0.9,I)}(t)$, respectively. The different return levels in each case have equivalent occurrence probabilities in the context of their respective phases of climatic oscillations.

Figure 20 shows half the width of the 95% confidence interval for 100-year return levels presented in the respective plots in Figure 19 based on 200 bootstrapped data sets. For each phase of SCV, we can see the most uncertainty inland, where we have the shortest records of data. Furthermore, among the three levels of SCV, most uncertainty occurs during high levels, which correspond to unusually cold events such as that of winter 2009/10.

Figure 21 shows how the estimated 100-year level derived from model E2 has changed since 1950 during different levels of SCV. In each case, we see that the largest increases are inland. The 100-year return level during levels of median SCV (centre plot; Figure 21) has increased between 2.1 – 3°C . This increase in extreme temperatures over the observed record is substantially larger than the approx 0.8 – 1°C change of $M^I(t)$ over the same period (see Figure 4). This result reiterates that climate

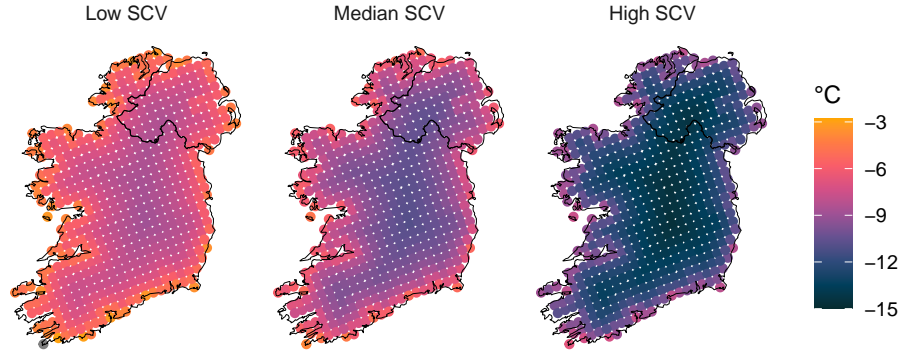


Figure 19: Estimated 100-year marginal return level in 2022 for (left-right) low, median, and high phases of SCV derived from model E2.

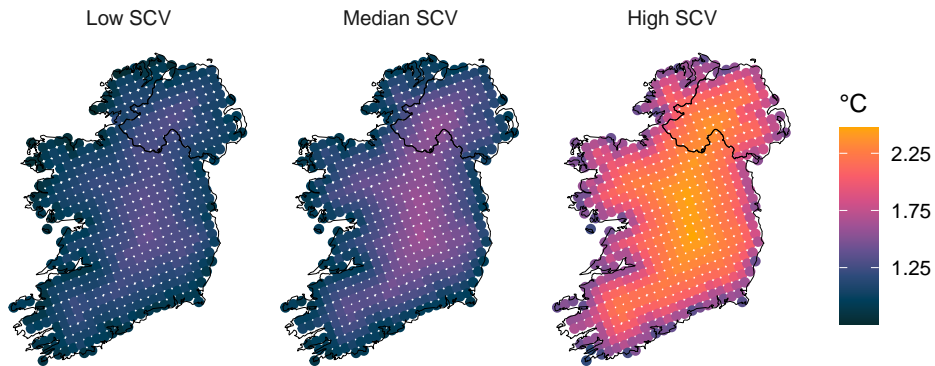


Figure 20: Half the width of the 95% confidence interval of 100-year return level in 2022 for low, median, and high phases (left-right) of SCV derived from model E2 from 200 spatio-temporal bootstraps.

change is more radically affecting extreme temperatures than mean temperatures. Furthermore, an increase of 2.1–3°C of the 100-year level is in contrast to the respectively lower increase of 1.2–2.2°C estimated for maximum summer 100-year levels over a similar period (1942–2020) (Healy et al., 2024). This indicates that winter extreme minimum temperatures are warming faster than summer extreme maximum temperatures, corroborating Ireland’s reflection of global trends. We see the most substantial increase in 100-year return levels is in the context of high SCV (right-hand plot; Figure 21) with an estimated increase of 2.9–4°C over the island. This suggests that climatic conditions that would typically result in very cold temperatures in Ireland are now resulting in much warmer temperatures. This aligns with the findings of Christiansen et al. (2018), which suggest that the winter of 2009/10 was much milder than expected given the climatic conditions at the time. We estimate the lowest levels of warming during the low phase of SCV (left-hand plot; Figure 21) with an increase 1.9–2.7°C over the island. Figure 22 reports the 95% confidence interval of changes in 100-year return levels calculated using 200 bootstrapped data sets. The columns in Figure 22 correspond to the respective column of Figure 21. The top row corresponds to the lower bound while the bottom row corresponds to the upper bound. At all three levels of SCV, and at all sites, the changes are positive.

We investigate the sensitivity of our threshold choice as discussed in Section 3.3.3. Figure 23 reports the difference between the 100-year level derived from our chosen model, E2, using our chosen threshold, $u^{(0.96)}(s)$, with 100-year levels estimated using a lower threshold (left-hand plot, with $\tau = 0.95$) and higher threshold (right-hand plot, with $\tau = 0.97$). The differences between the return level estimates are well within the 95% uncertainty interval of our chosen estimate. This suggests that while

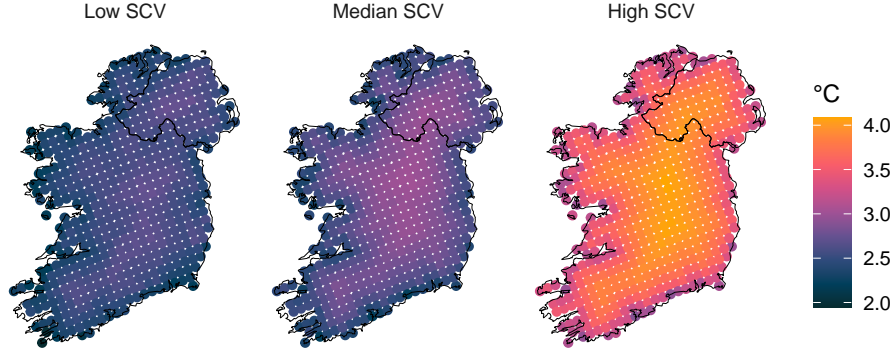


Figure 21: Estimated change in 100-year marginal return level over the period 1950–2022 for low, median, and high phases (left-right) of SCV derived from model E2.

there is a small difference in return levels estimated with slightly different thresholds, these differences are captured by our bootstrapped uncertainties.

5.2 Spatial results

To derive summary statistics of spatial extreme events, we first generate a database of spatial extreme simulations and present empirically estimated risk measures using these simulations. We first simulate an event from the r -Pareto process, on Pareto margins, and then back transform this to the data scale using the inverse of expression (5). As the r -Pareto process is stationary over time, we can generate identical events in Pareto margins to transform to any specific time and any phase of SCV using the time-varying model E2. The r -Pareto process simulations are generated using the R package `mvPot` (de Fondeville et al., 2021), which exploits the decomposition in (9). Point estimates of the spatial risk summaries are based on 100,000 simulations, for each phase of the SCV. Uncertainties are based on 10,000 simulations for each r -Pareto process fitted to each of the 200 spatio-temporal bootstrap data sets, totalling an additional 200,000 simulations for each phase of SCV.

We are most interested in making inferences about spatial events of the observational process that exceed a critical temperature of $T^\circ\text{C}$ somewhere over Ireland at time t . We denote these events by

$$A_{t,\mathcal{S}}(T) = \{X_o^P(t, \mathbf{s}), \mathbf{s} \in \mathcal{S} : \exists \mathbf{s}_0 \in \mathcal{S} \text{ with } X_o^P(t, \mathbf{s}_0) < T^P(t, \mathbf{s}_0)\}, \quad (11)$$

where $T^P(t, \mathbf{s})$ is the mapping of T through the transformation (5) at time t and for site \mathbf{s} . Recall that we are modelling negated minimum daily temperatures, so the set $A_{t,\mathcal{S}}(T)$ in (11), corresponds to extremely cold temperatures. To estimate $\Pr\{A_{t,\mathcal{S}}(T)\}$ we use an importance sampling procedure proposed by Healy et al. (2024). Specifically, we take

$$\widehat{\Pr}_{imp}\{A_{t,\mathcal{S}}(T)\} = \frac{1}{b_{T(t)}mL} \sum_{i=1}^m \sum_{j=1}^L I\left\{\exists \mathbf{s}_0 \in \mathcal{S} : r_j^P b_{T(t)} \frac{y_i^P(\mathbf{s}_0)}{r_i} > T^P(t, \mathbf{s}_0)\right\}, \quad (12)$$

where $b_{T(t)} = \min_{\mathbf{s} \in \mathcal{S}} \{T^P(t, \mathbf{s})/\omega_{(m)}(\mathbf{s})\}$ and L is taken as large as possible to improve computational efficiency. We found that taking $L = 300$ provided satisfactorily smooth estimates while achieving computational efficiency. With this scaling choice, and the extrapolation from the $r_j^P > \max(r_1, \dots, r_m)$, we are guaranteed to have at least L out of the mL simulated fields which achieve at least temperature $T^\circ\text{C}$ somewhere in \mathcal{S} in year t . Estimates of $\Pr\{A_{t,\mathcal{S}}(T)\}$ for a range of extremal temperatures $T \in [-20, -5]$ for years 1950 and 2022 and for different phases of SCV are given in Figure 24.

Rohan (1986) notes that a temperature of -10°C is an extremely cold temperature in Ireland and is in the coldest 1 percentile of daily temperature minima. Our model finds that the spatial event

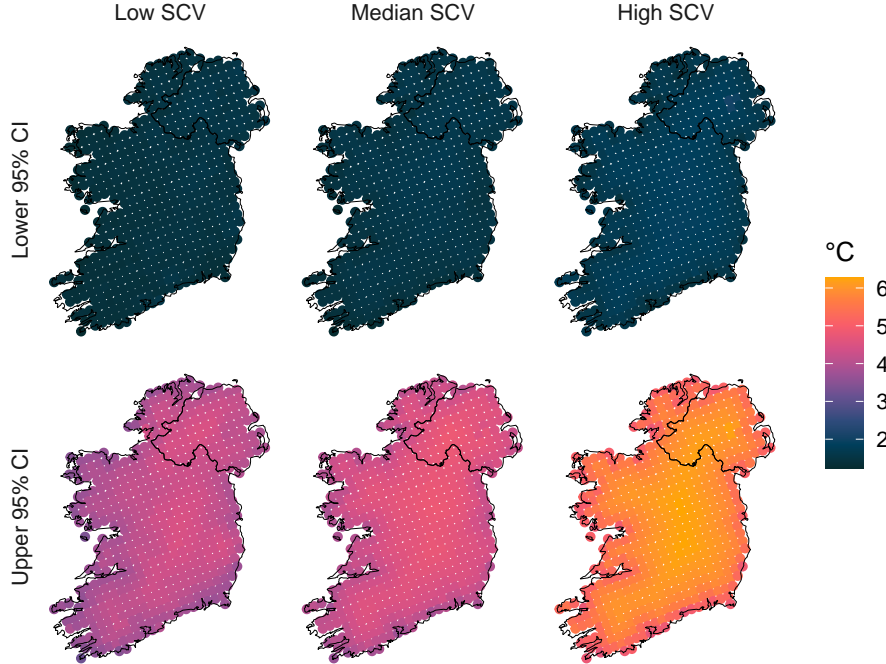


Figure 22: The lower bound of 95% confidence interval of change in 100-year return level according to model E2 for low, median, and high phases of SCV (top row, left to right respectively). The upper bound of 95% confidence interval of the corresponding plot in the top row (bottom row). Confidence intervals are based on 200 bootstrapped data sets.

$A_{t,\mathcal{S}}(-10)$ has increased from a 1 in 0.2-year to a 1 in 0.7-year event in high phases of SCV, a 1 in 1.4-year to a 1 in 1-12 year event in median phases of SCV and a 1 in 5-year to a 1 in 70-year event in low phases of SCV. If we consider the coldest temperature in the republic of Ireland, observed in the winter of 2009/10, which was -17.5°C on the 25th of December 2010 in Co. Mayo, the spatial event $A_{t,\mathcal{S}}(-17.5)$ changed from approximately a 1 in 10-year event in 1950 to a 1 in 370-year event in 2022 in the context of a high phase of SCV. Regarding the coldest temperature in recorded history on the island of Ireland of -19.4°C recorded at Omagh, Co. Tyrone on the 23rd of January 1881 (Hickey, 2011), the spatial event $A_{t,\mathcal{S}}(-19.4)$ changes from being a 1 in 38-year event in 1950 to a 1 in 3,700-year event in 2022, in the context of a high phase of SCV. However, note that a temperature of this extremity is not in our data set so estimates are very uncertain.

Our simulation strategy allows us to generate replicated independent spatial fields which exceed $T^\circ\text{C}$ for at least one $s \in \mathcal{S}$. This is essentially achieved by exploiting the decomposition in (9) to scale simulations by multiplying R with a known change in probability of occurrence, i.e., $\Pr\{A_{t,\mathcal{S}}(T)\}$ as estimated above. We scale simulations to be below temperature $T^\circ\text{C}$ for at least one site. Estimates of the following risk measures are calculated on the scaled simulations, following this the estimates are rescaled to interpretable levels. Firstly, we investigate the behaviour of the “data scale χ ”, which combines the effect of changes in the marginal distributions over time with the estimated extremal dependence structure,

$$\chi_o(h; T, t) = \Pr(\exists \mathbf{s}_0 \in \mathcal{S} : \min[X_o(t, \mathbf{s}_0), X_o(t, \mathbf{s}^h)] > T),$$

where \mathbf{s}^h is a randomly selected site in \mathcal{S} with $\|\mathbf{s}^h - \mathbf{s}_0\| = h$. Since we are working with negated temperatures, this corresponds to two sites, distance h apart both being below a temperature T . Figure 25 presents estimates of this risk measure for a range of h and $T = \{-8, -9, -10\}$, between

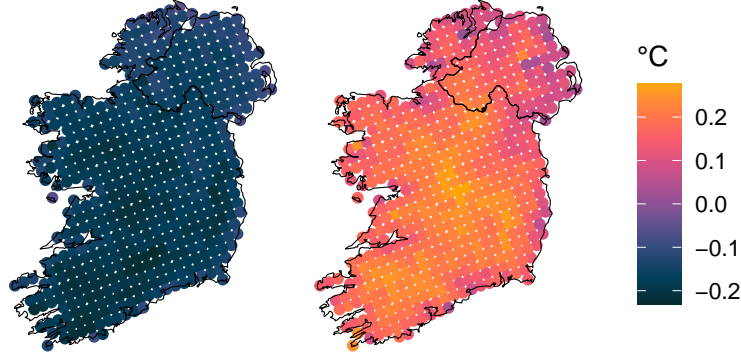


Figure 23: The difference in the 100-year level during the median phase of SCV in 2022 between model E2 fit to exceedances above the chosen threshold of $u^{(0.96)}(\mathbf{s})$ and to exceedances above both a lower threshold of $u^{(0.95)}(\mathbf{s})$ (left) and higher threshold of $u^{(0.97)}(\mathbf{s})$ (right).

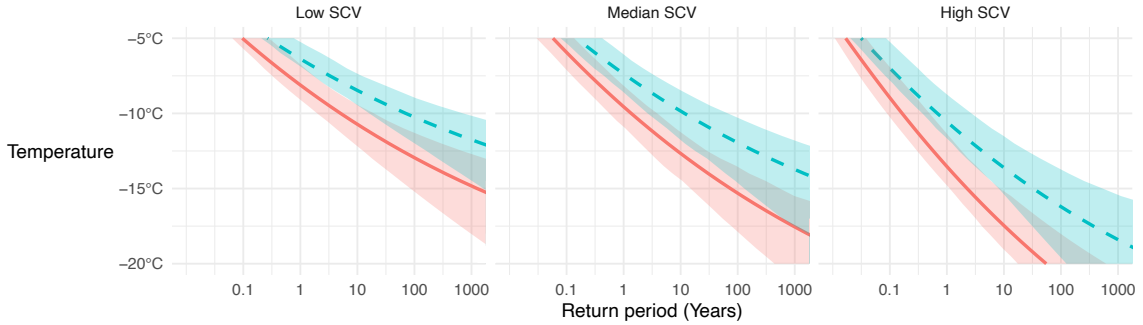


Figure 24: Return period of the event $A_{t,S}(T)$ where an extreme temperature exceeding $T^\circ\text{C}$ occurs somewhere on the Irish station network, \mathcal{S}_o . Blue dashed (solid orange) lines correspond to $t = 2022$ (1950). Shaded regions show pointwise 95% confidence intervals for the return periods at low, median, and high SCV from left-right.

1950 and 2022. Our analysis indicates a consistent pattern across the three phases of SCV. We observe a higher likelihood of joint cold extreme temperatures occurring at greater distances during earlier periods. As temperatures become increasingly extreme, there is a tendency for them to become more localised. Additionally, the probability of joint extreme temperature events is greater during periods of high phases of SCV, even at the furthest distances. We note that the uncertainties associated with these findings exhibit a high degree of noise. This is primarily due to the substantial computational resources required for generating and storing simulations for calculating this statistic. The computational burden is increased as we are interested in making inferences at different levels of climatic variability. We report uncertainty as the 95% quantiles of $\chi_o(h; T, t)$ in bins of 25km. For $\chi_o(h; T, t)$ we see that the joint probability of temperature being below T at sites h apart changes notably with time, e.g., taking $h = 100$ km, we find that $\chi_o(h; T, t)$ has increased by a factor of 7.4, 13.7, and 24.2 for $T = -8, -9,$ and -10°C , respectively, during the low phase of SCV. The respective equivalent estimates for median and high phases of SCV are 4.7, 6.9, 11.9 and 2.8, 3.3, 3.9. Notice that we see the smallest increases during the highest phase of SCV, this is due to the fact that extremely low temperatures are much more likely to occur in these periods, and so these temperatures are much farther into the tail of the GPD in phases of low SCV.

Finally, in Figure 26 we look at a fully spatial risk measure on the station network over Ireland from 1950 to 2022. This figure plots the expected proportion of a temperature field on \mathcal{S} , which exceeds

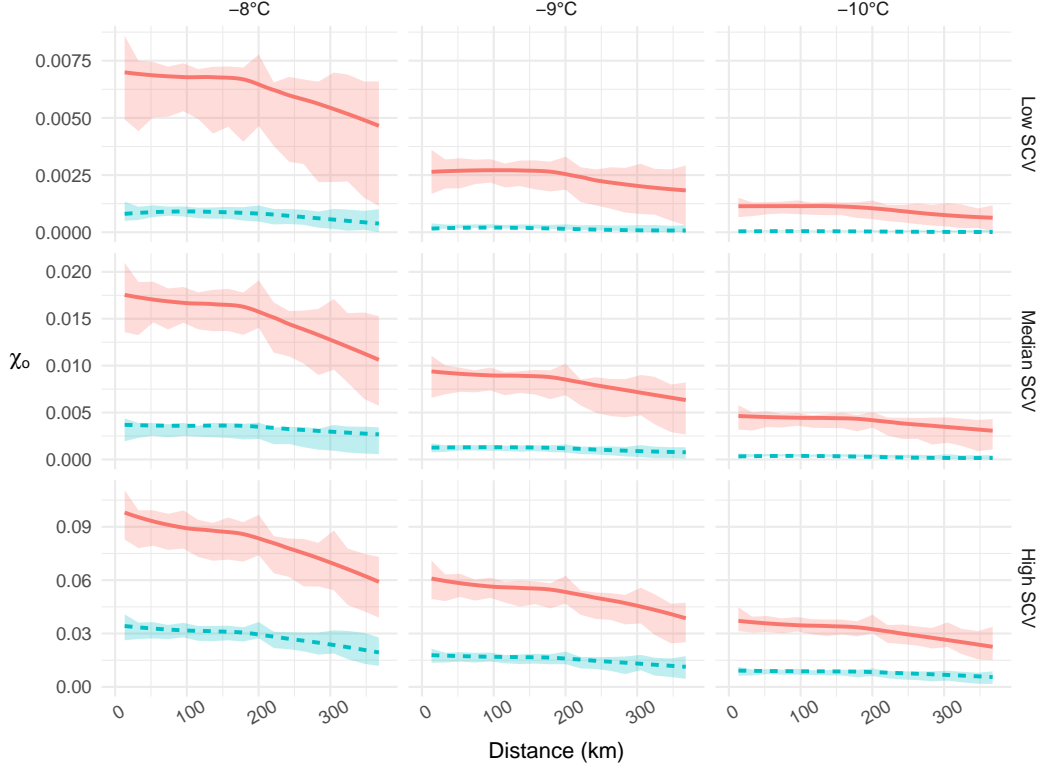


Figure 25: Estimates of $\chi_o(h; T, t)$ against h (in km) for $T = -8, -9,$ and -10°C (left-right respectively) for 1950 (solid, orange line) and for 2022 (dashed, blue line) for model E2 at low, median, and high levels of SCV (top to bottom row respectively). Confidence intervals are based on 10,000 simulations for each 200 bootstrap sample data set and each level of SCV.

$T^\circ\text{C}$, i.e., it plots $E_o^D(T; t)$ against T , defined as:

$$E_o(C; t, T) = \text{E} \left(\frac{1}{|\mathcal{S}|} \int_{\mathcal{S}} I\{X_o(t, \mathbf{s}) > T\} d\mathbf{s} \right) \quad (13)$$

where $I(B)$ is the indicator function of event B . Again, since data is negated, $E_o(C; t, T)$ corresponds to the expected proportion of sites that are colder than temperature T . The figure shows that the relative change in spatial extent over this period decreases with more extreme cold temperatures T . Figure 26 shows that for $T = -10^\circ\text{C}$, estimates of $E_o(C; t, T)$ have decreased by a factor of 17.2, 10.2, and 4.68 in phases of low, median, and high SCV. This indicates that events are becoming more localised at all phases of SCV.

6 Conclusion & discussion

The aim of this research was to identify and characterise non-stationarities of extremely cold daily winter temperatures in Ireland. Given the complex and variable nature of extreme minimum winter temperatures, we emphasise the importance of considering the climatic context (i.e., the atmospheric and oceanic patterns) in which they occur. Specifically, we discuss how shifts in the jet stream's behaviour can lead to the increased occurrence of extremely cold winter temperatures. We have presented some novel candidate approaches to account for large variations in cold extremes during different phases of large-scale climatic patterns. We explore using NAO and AO indices as covariates to help explain the behaviour of the jet stream and its impact on weather patterns. However, we find that using the HadCRUT5 data set, which combines land and sea surface temperature anomalies, best

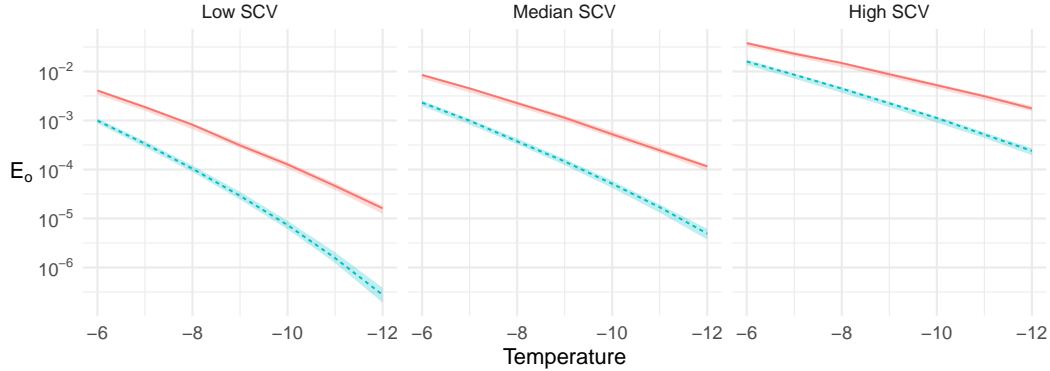


Figure 26: Expected proportion, $E_o(C; t, T)$, of Ireland that exceeds a temperature of $T^\circ\text{C}$ in an extreme event given that at least one site in Ireland (at the station network) exceeds $T^\circ\text{C}$ according to E2 for low, median, and high levels of SCV (left to right, respectively) in 1950 (solid, orange line) and 2022 (dashed, blue line). Confidence intervals are based on 10,000 simulations for each 200 bootstrap sample data set and each level of SCV.

captures and represents all climatic processes driving extremely cold temperatures. Furthermore, we show that not accounting for this climatic variability conflates unusually cold winter events with the contrasting general trend of warming winters, and underestimates long-term warming trends.

We have presented a method of characterising and visualising climate risk associated with different phases of what we define as “short-term climatic variability” (SCV). We have developed a novel bootstrapping approach (used to account for uncertainty throughout) to accommodate the stronger temporal dependence and complex variability observed in extremely cold winter events, as compared to hot summer events. We found that the climate model data were less helpful as a covariate for the GPD as compared to the case for maximum daily summer temperatures. However, for non-extreme minimum daily summer temperatures, the climate model output proved informative and helpful.

Our study reveals that, across Ireland, there has been a decrease in the frequency and intensity of extremely cold temperatures since 1950. Furthermore, the rate of warming of extreme minimum temperatures is substantially greater than that of maximum summer temperatures (Healy et al., 2024). Overall, the analysis reveals there has been a decrease in the frequency and intensity of extremely cold temperatures since 1950 in Ireland, with the largest changes observed in regions further inland, during all phases of SCV considered.

We found that from 1950 to 2022 the occurrence rates of high threshold exceedances have decreased for each phase of SCV. We found that extreme quantiles have increased by 2–4°C, over different phases of SCV. We describe changes in spatial risk over time, combining both marginal and dependence features. We found that spatial cold events have become more localised, with this change increasing at more extreme temperatures, and greatest for low phases of SCV. Overall, spatial cold extreme events are becoming less frequent and warmer over time.

7 Funding and Acknowledgements

Healy’s work was supported by SFI grant 18/CRT/6049. This study was also carried out within the RISE project and received funding from the European Union Next-GenerationEU - National Recovery and Resilience Plan (NRRP) – MISSION 4 COMPONENT 2, INVESTIMENT 1.1 Fondo per il Programma Nazionale di Ricerca e Progetti di Rilevante Interesse Nazionale (PRIN) – CUP N.H53D23002010006. This publication reflects only the authors’ views and opinions, neither the European Union nor the European Commission can be considered responsible for them. Andrew Parnell’s work was supported by: the UCD-Met Éireann Research Professorship Programme (28-UCDNWPAI);

a Research Ireland Research Centre award 12/RC/2289.P2; the Research Ireland Centre for Research Training 18CRT/6049; and Research Ireland Co-Centre Climate+ in Climate Biodiversity and Water award 22/CC/11103. We thank Simon Noone (Maynooth University) for help with data. For access to climate data, we acknowledge the World Climate Research Programme’s Working Groups on Regional Climate and on Coupled Modelling, and the European Network for Earth System Modelling. For the purpose of Open Access, the authors have applied a CC BY public copyright licence to any Author Accepted Manuscript version arising from this submission.

References

- Bai, Y., Song, P. X.-K., and Raghunathan, T. E. (2012). Joint composite estimating functions in spatiotemporal models. *Journal of the Royal Statistical Society: Series B (Statistical Methodology)*, 74:799–824.
- Ballester, J., Quijal-Zamorano, M., Turrubiates, R. F. M., Pegenaute, F., Herrmann, F. R., Robine, J. M., Basagaña, X., Tonne, C., Antó, J. M., and Achebak, H. (2023). Heat-related mortality in europe during the summer of 2022. *Nature Medicine*, 29:1857–1866.
- Banerjee, S., Carlin, B. P., and Gelfand, A. E. (2014). *Hierarchical Modeling and Analysis for Spatial Data*. Chapman & Hall/CRC.
- Bindi, M. and Olesen, J. E. (2011). The responses of agriculture in europe to climate change. *Regional Environmental Change*, 11:151–158.
- Boucek, R. E., Gaiser, E. E., Liu, H., and Rehage, J. S. (2016). A review of subtropical community resistance and resilience to extreme cold spells. *Ecosphere*, 7.
- Cattiaux, J., Vautard, R., Cassou, C., Yiou, P., Masson-Delmotte, V., and Codron, F. (2010). Winter 2010 in europe: a cold extreme in a warming climate. *Geophysical Research Letters*, 37.
- Chavez-Demoulin, V. and Davison, A. C. (2005). Generalized additive modelling of sample extremes. *Journal of the Royal Statistical Society: Series C (Applied Statistics)*, 54:207–222.
- Christiansen, B. O., Alvarez-Castro, C., Christidis, N., Ciavarella, A., Colfescu, I., Cowan, T., Eden, J., Hauser, M., Hempelmann, N., Klehmet, K., Lott, F., Nangini, C., Oldenborgh, G. J. V., Orth, R., Stott, P., Tett, S., Vautard, R., Wilcox, L., and Yiou, P. (2018). Was the cold european winter of 2009/10 modified by anthropogenic climate change? an attribution study. *Journal of Climate*, 31:3387–3410.
- Coles, S. G., Heffernan, J. E., and Tawn, J. A. (1999). Dependence measures for extreme value analyses. *Extremes*, 2:339–365.
- Conlon, K. C., Rajkovich, N. B., White-Newsome, J. L., Larsen, L., and O’Neill, M. S. (2011). Preventing cold-related morbidity and mortality in a changing climate.
- Davison, A. C. and Smith, R. L. (1990). Models for exceedances over high thresholds (with discussion). *Journal of the Royal Statistical Society: Series B (Statistical Methodology)*, 52:393–442.
- de Fondeville, R., Belzile, L., and Thibaud, E. (2021). mvpot: multivariate peaks-over-threshold modelling for spatial extreme events.
- de Fondeville, R. and Davison, A. C. (2018). High-dimensional peaks-over-threshold inference. *Biometrika*, 105:575–592.

- Deser, C. (2000). On the teleconnectivity of the arctic oscillation. *Geophysical Research Letters*, 27:779–782.
- Dombry, C. and Ribatet, M. (2015). Functional regular variations, pareto processes and peaks over threshold. *Statistics and its Interface*, 8:9–17.
- Donat, M. G., Sillmann, J., Wild, S., Alexander, L. V., Lippmann, T., and Zwiers, F. W. (2014). Consistency of temperature and precipitation extremes across various global gridded in situ and reanalysis datasets. *Journal of Climate*, 27:5019–5035.
- Dunn, R. J. H., Alexander, L. V., Donat, M. G., Zhang, X., Bador, M., Herold, N., Lippmann, T., Allan, R., Aguilar, E., Barry, A. A., Brunet, M., Caesar, J., Chagnaud, G., Cheng, V., Cinco, T., Durre, I., Guzman, R., Htay, T. M., Ibadullah, W. M. W., Ibrahim, M. K. I. B., Khoshkam, M., Kruger, A., Kubota, H., Leng, T. W., Lim, G., Li-Sha, L., Marengo, J., Mbatha, S., McGree, S., Menne, M., Skansi, M. M., Ngwenya, S., Nkrumah, F., Oonariya, C., Pabon-Caicedo, J. D., Panthou, G., Pham, C., Rahimzadeh, F., Ramos, A., Salgado, E., Salinger, J., Sané, Y., Sopaheluwakan, A., Srivastava, A., Sun, Y., Timbal, B., Trachow, N., Trewin, B., Schrier, G., Vazquez-Aguirre, J., Vasquez, R., Villarroel, C., Vincent, L., Vischel, T., Vose, R., and Yussof, M. N. B. H. (2020). Development of an updated global land in situ-based data set of temperature and precipitation extremes: Hadex3. *Journal of Geophysical Research: Atmospheres*, 125:e2019JD032263.
- Engelke, S., Malinowski, A., Kabluchko, Z., and Schlather, M. (2015). Estimation of hüsler–reiss distributions and brown-resnick processes. *Journal of the Royal Statistical Society: Series B (Statistical Methodology)*, 77:239–265.
- Francis, J. A. and Vavrus, S. J. (2012). Evidence linking arctic amplification to extreme weather in mid-latitudes. *Geophysical Research Letters*, 39.
- García, C., C.A, W., Dwyer, N., and Gault, J. (2022). Climate status report for ireland 2020.
- Gerber, E. P. and Vallis, G. K. (2009). On the zonal structure of the north atlantic oscillation and annular modes. *Journal of the Atmospheric Sciences*, 66:332–352.
- Giorgi, F. (2019). Thirty years of regional climate modeling: where are we and where are we going next? *Journal of Geophysical Research: Atmospheres*, 124:5696–5723.
- Gneiting, T. and Katzfuss, M. (2014). Probabilistic forecasting. *Annual Review of Statistics and Its Application*, 1:125–151.
- Gupta, A. S. and McNeil, B. (2012). *Variability and change in the ocean*, pages 141–165. Elsevier.
- Hall, R., Erdélyi, R., Hanna, E., Jones, J. M., and Scaife, A. A. (2015). Drivers of north atlantic polar front jet stream variability. *International Journal of Climatology*, 35:1697–1720.
- Hastie, T., Tibshirani, R., and Friedman, J. (2009). *The Elements of Statistical Learning*, volume 27. Springer, 2 edition.
- He, Y., Fang, J., Xu, W., and Shi, P. (2022). Substantial increase of compound droughts and heatwaves in wheat growing seasons worldwide. *International Journal of Climatology*, 42:5038–5054.
- Healy, D., Tawn, J., Thorne, P., and Parnell, A. (2024). Inference for extreme spatial temperature events in a changing climate with application to ireland (with discussion). *Journal of the Royal Statistical Society: Series C [to appear]*, page qlae047.

- Hickey, K. (2011). The historic record of cold spells in ireland. *Irish Geography*, 44:303–321.
- Hooker, K. V., Coxon, C. E., Hackett, R., Kirwan, L. E., O’Keeffe, E., and Richards, K. (2008). Evaluation of cover crop and reduced cultivation for reducing nitrate leaching in ireland. *Journal of Environmental Quality*, 37:138–145.
- Hoskins, B. J. and James, I. N. (2014). *Fluid Dynamics of the Midlatitude Atmosphere*. John Wiley & Sons, Ltd.
- Hüsler, J. and Reiss, R.-D. (1989). Maxima of normal random vectors: between independence and complete dependence. *Statistics and Probability Letters*, 7:283–286.
- Ip, R. H. L. and K., L. W. (2017). On some matérn covariance functions for spatio-temporal random fields. *Statistica Sinica*, 27:805–822.
- IPCC (2021). *The Physical Science Basis. Contribution of Working Group I to the Sixth Assessment Report of the Intergovernmental Panel on Climate Change*, pages 2061–2086. Cambridge University Press.
- Kennedy, J. J., Rayner, N. A., Atkinson, C. P., and Killick, R. E. (2019). An ensemble data set of sea surface temperature change from 1850: The met office hadley centre hadsst.4.0.0.0 data set. *Journal of Geophysical Research: Atmospheres*, 124:7719–7763.
- Kidston, J., Scaife, A. A., Hardiman, S. C., Mitchell, D. M., Butchart, N., Baldwin, M. P., and Gray, L. J. (2015). Stratospheric influence on tropospheric jet streams, storm tracks and surface weather. *Nature Geoscience*, 8:433–433.
- Liou, K. N. (2002). *Solar radiation at the top of the atmosphere*, pages 37–64. Academic Press.
- Mateus, C. and Coonan, B. (2022). Isotherman maps of maximum and minimum shade air temperatures in ireland.
- Matthes, H., Rinke, A., and Dethloff, K. (2015). Recent changes in arctic temperature extremes: warm and coldspells during winter and summer. *Environmental Research Letters*, 10:114020.
- McElwain, L. and Sweeney, J. (2003). Climate change in ireland- recent trends in temperature and precipitation. *Irish Geography*, 36:97–111.
- Met Office (2012). Met office integrated data archive system (midas) land and marine surface stations data (1853-current).
- Met Éireann (2019). Winter report 2018/19.
- Morice, C. P., Kennedy, J. J., Rayner, N. A., Winn, J. P., Hogan, E., Killick, R. E., Dunn, R. J., Osborn, T. J., Jones, P. D., and Simpson, I. R. (2021). An updated assessment of near-surface temperature change from 1850: The hadcrut5 dataset. *Journal of Geophysical Research: Atmospheres*, 126:e2019JD032361.
- Nolan, P. and Flanagan, J. (2020). High-resolution climate projections for ireland-a multi-model ensemble approach.
- Oldenborgh, G. J. V., Mitchell-Larson, E., Vecchi, G. A., Vries, H. D., Vautard, R., and Otto, F. (2019). Cold waves are getting milder in the northern midlatitudes. *Environmental Research Letters*, 14.

- Osborn, T. J., Jones, P. D., Lister, D. H., Morice, C. P., Simpson, I. R., Winn, J. P., Hogan, E., and Harris, I. C. (2021). Land surface air temperature variations across the globe updated to 2019: the crutem5 data set. *Journal of Geophysical Research: Atmospheres*, 126:e2019JD032352.
- Osland, M. J., Stevens, P. W., Lamont, M. M., Brusca, R. C., Hart, K. M., Waddle, J. H., Langtimm, C. A., Williams, C. M., Keim, B. D., Terando, A. J., Reyier, E. A., Marshall, K. E., Loik, M. E., Boucek, R. E., Lewis, A. B., and Seminoff, J. A. (2021). Tropicalization of temperate ecosystems in north america: The northward range expansion of tropical organisms in response to warming winter temperatures. *Global Change Biology*, 27:3009–3034.
- Palacios-Rodríguez, F., Toulemonde, G., Carreau, J., and Opitz, T. (2020). Generalized pareto processes for simulating space-time extreme events: an application to precipitation reanalyses. *Stochastic Environmental Research and Risk Assessment*, 34:2033–2052.
- Perkins-Kirkpatrick, S. E. and Lewis, S. C. (2020). Increasing trends in regional heatwaves. *Nature Communications*, 11:3357.
- Rohan, P. K. (1986). *The climate of Ireland*. Stationery Office, 2 edition.
- Screen, J. A. and Simmonds, I. (2014). Amplified mid-latitude planetary waves favour particular regional weather extremes. *Nature Climate Change* 2014 4:8, 4:704–709.
- Service, C. C. C. (2019). Cordex regional climate model data on single levels.
- Sippel, S., Barnes, C., Cadiou, C., Fischer, E., Kew, S., Kretschmer, M., Philip, S., Shepherd, T. G., Singh, J., Vautard, R., and Yiou, P. (2024). Could an extremely cold central european winter such as 1963 happen again despite climate change? *Weather and Climate Dynamics*, 5:943–957.
- Skendžić, S., Zovko, M., Živković, I. P., Lešić, V., and Lemić, D. (2021). The impact of climate change on agricultural insect pests.
- Sousa, P. M., Trigo, R. M., Barriopedro, D., Soares, P. M., and Santos, J. A. (2018). European temperature responses to blocking and ridge regional patterns. *Climate Dynamics*, 50:457–477.
- Stendel, M., Francis, J., White, R., Williams, P. D., and Woollings, T. (2021). *The jet stream and climate change*, pages 327–357. Elsevier.
- Team, R. C. (2023). R: A language and environment for statistical computing. <https://www.R-project.org>.
- Thompson, D. W. and Wallace, J. M. (2001). Regional climate impacts of the northern hemisphere annular mode. *Science*, 293:85–89.
- Thompson, D. W. J. and Wallace, J. M. (1998). The arctic oscillation signature in wintertime geopotential height and temperature fields. *Geophysical Research Letters*, 25:1297–1300.
- Vihma, T., Graverson, R., Chen, L., Handorf, D., Skific, N., Francis, J. A., Tyrrell, N., Hall, R., Hanna, E., Uotila, P., Dethloff, K., Karpechko, A. Y., Björnsson, H., and Overland, J. E. (2020). Effects of the tropospheric large-scale circulation on european winter temperatures during the period of amplified arctic warming. *International Journal of Climatology*, 40:509–529.